Draft version August 8, 2022
Typeset using LaTeX default style in AASTeX631

The Sun's Mean Line-of-Sight Field

Neil R. Sheeley, Jr.[1]

[1] *Visiting Research Scientist*
Lunar and Planetary Laboratory, University of Arizona
Tucson, AZ 85721, USA

ABSTRACT

We regard the Sun-as-a-star magnetic field (*i.e.* the mean field) as a filter for the spherical harmonic components of the photospheric field, and calculate the transmission coefficients of this filter. The coefficients for each harmonic, Y_l^m, are listed in three tables according to their dependence on B_0, the observer's latitude in the star's polar coordinate system. These coefficients are used to interpret the 46-yr sequence of daily mean-field measurements at the Wilcox Solar Observatory. We find that the non-axisymmetric part of the field originates in the Y_1^1, Y_2^2, and a combination of the Y_3^3 and Y_3^1 harmonic components. The axisymmetric part of the field originates in Y_2^0 plus a B_0-dependent combination of the Y_1^0 and Y_3^0 components. The power spectrum of the field has peaks at frequencies corresponding to the ∼27-day synodic equatorial rotation period and its second and third harmonics. Each of these peaks has fine structure on its low-frequency side, indicating magnetic patterns that rotate slowly under the influence of differential rotation and meridional flow. The sidebands of the fundamental mode resolve into peaks corresponding to periods of ∼28.5 and ∼30 days, which tend to occur at the start of sunspot maximum, whereas the ∼27-day period tends to occur toward the end of sunspot maximum. We expect similar rotational sidebands to occur in magnetic observations of other Sun-like stars and to be a useful complement to asteroseismology studies of convection and magnetic fields in those stars.

Keywords: Solar magnetic fields (1503)— Solar rotation (1524),—Solar cycle (1487)— Stellar magnetic fields (1610)

1. INTRODUCTION

The Sun's mean line-of-sight field is obtained by averaging the line-of-sight component of the photospheric magnetic field over the (flat) solar disk. The measurement is obtained from Earth, sometimes in integrated sunlight, and is often called the 'Sun-as-a-star' magnetic field, as if the observation were obtained from the even greater distance of another star.

In the early 1970s, John Wilcox proposed to build a new solar telescope in the hills south of the Stanford University campus. The telescope would have relatively coarse spatial resolution ∼1 arcmin and the capability of measuring the Sun's mean line-of-sight field. The idea was not to compete with the telescopes at Mount Wilson and Kitt Peak, which were already obtaining daily observations of the solar disk with much higher spatial resolution, but instead to concentrate on factors like sensitivity and zero-point stability to produce a long-term sequence of relatively precise, global observations that could be used to study the Sun's large-scale field.

Wilcox and Ness had discovered the interplanetary sector structure using spacecraft data from the Interplanetary Monitoring Platform (IMP) (Wilcox & Ness 1965a,b; Ness & Wilcox 1965). Also, by comparing those IMP spacecraft data with photospheric magnetograms obtained at the Mount Wilson Observatory (MWO), Wilcox and Robert Howard had shown that the sector structure originated in long-lived, unipolar magnetic regions on the Sun (Wilcox & Howard 1968). Consequently, Wilcox thought that mean field observations would be important for solar-terrestrial studies and, in particular, would help to improve the ∼4.5-day timing between the central meridian passage of a sector boundary at the Sun and at the Earth. (See the discussion following Douglas Jones's talk at the Second Solar Wind Conference (Jones 1972).) As pointed out by Scherrer et al. (1977a), Kotov and Severny had already begun daily observations of the mean field at the Crimean Observatory in 1968, and Robert Howard began them at the Mount Wilson Observatory

in 1970. So Wilcox's interest in what we now call 'space weather' was the motivation for building the Stanford Solar Observatory[1].

Wilcox's proposal was accepted and daily measurements of the Sun-as-a-star field began on May 16, 1975. These measurements were obtained in 'integrated sunlight' using a 2.7 m focal length objective lens that creates a 2.5 cm solar image located 3.8 m above the entrance slit of the spectrograph (Scherrer et al. 1977a). The new observations quickly confirmed that the strength of the mean field is correlated with the central-meridian-passage time of low-latitude coronal holes and with the associated pattern of interplanetary sectors (Scherrer et al. 1976, 1977b; Sheeley et al. 1976). In addition, 27-day Bartels displays of the WSO mean-field measurements matched the corresponding displays of mean field calculated using the flux-transport model. This provided one of the first verifications of the transport model and showed that the mean field originated in flux that spread out from its sources in active regions (Sheeley et al. 1985; Sheeley & DeVore 1986a,b). Many years later, we learned that the mean-field correlates with the occurrence of coronal inflows seen with white-light coronagraphs on the Solar and Heliospheric Observatory (SOHO) and Solar Terrestrial Relations Observatory (STEREO) spacecraft (Sheeley & Wang 2015).

The reason for these correlations is that the mean field is an approximate measure of the Sun's non-axisymmetric field, and, in particular, of its horizontal dipole and quadrupole components, Y_1^1 and Y_2^2. These non-axisymmetric fields are strengthened by the emergence of flux in active regions, whose bright coronal extensions provide backgrounds for seeing the much fainter inflows that rain downward from reconnection sites in the outer corona (Sanchez-Diaz et al. 2017; Wang & Hess 2018). The outward components of these reconnections are sometimes observed as streamer blobs moving out through the $30R_\odot$ field of view like 'leaves in the wind' and gradually swept up by high speed streams to form regions of high density (Sheeley et al. 2008a,b; Sheeley & Rouillard 2010).

The purpose of this paper is to analyze an idealized Sun-as-a-star field into its spherical harmonic components to determine the ones that ought to contribute (both for the Sun and for a distant star), and then to decompose (or demodulate) the observed WSO mean field to find out what those contributions have been since the observations began in 1975. Although unknown to Wilcox in the early 1970s, the extension of these techniques to other Sun-like stars may complement asteroseismology and exoplanet studies.

2. THEORETICAL ANALYSIS OF THE MEAN FIELD

2.0.1. *Definition of the Field*

Let's begin with a definition for the mean line-of-sight field, B_m. In general, it is just the average of the line-of-sight field over the flat solar disk of radius, R:

$$B_m \;=\; \int B_{los} dA_{disk}/\pi R^2. \tag{1}$$

However, we would like to convert to an integral of the radial field, B_r, over the surface area A_{surf} of the Sun. In that case, we need two factors of $\sin\theta\cos\phi$ – one factor to convert B_{los} to B_r, and the other factor to convert dA_{los} to dA_{surf}. Also, we note that θ and ϕ are the usual polar and azimuthal angles in a spherical coordinate system with the x-axis pointing toward Earth. Therefore, Eq(1) becomes

$$B_m \;=\; \int B_{los} dA_{disk}/\pi R^2 \;=\; \int B_r(\sin\theta\cos\phi)^2 dA_{surf}/\pi R^2 \;=\; (1/\pi)\int_{-\pi/2}^{\pi/2}\int_0^{\pi} B_r(\sin\theta\cos\phi)^2\sin\theta d\theta d\phi, \tag{2}$$

where θ runs from 0 to π, and ϕ runs from $-\pi/2$ to $+\pi/2$. It is interesting to note that $\sin\theta\cos\phi$ is the axisymmetric quantity that is usually called μ in theories of line formation. So μ is 1 at disk center, 0 at the solar limb, and B_r is heavily weighted toward disk center as

$$B_m \;=\; \int B_r \mu^2 dA_{surf}/\pi R^2. \tag{3}$$

As discussed by Scherrer et al. (1977a), the weighting toward disk center is even greater for the WSO observations due to solar limb darkening and diffraction from the entrance slit of the spectrograph. In the Appendix of this paper, we consider the limb darkening in detail and find that the same harmonic components contribute to the mean field for a so-called gray atmosphere in the Eddington approximation as would occur in the absence of limb darkening. However,

[1] The observatory was renamed the Wilcox Solar Observatory (WSO) in 1983 when John Wilcox died while swimming in Mexico

the limb darkening reduces the strengths of the $l = 1$ and $l = 2$ components by 12%, and 3.75%, respectively, and increases the strength of the much weaker $l = 3$ components by 22%.

Up to this point, I have ignored the 7.25° tilt of the Sun's axis away from the normal to the ecliptic plane. We can include this effect by replacing $\sin\theta\cos\phi$ with $\sin\theta\cos\phi\cos B_0 + \cos\theta\sin B_0$, where B_0 is Earth's heliolatitude and varies annually from $-7.25°$ in February-March to $+7.25°$ in August-September. In that case, B_m becomes

$$B_m \;=\; (1/\pi)\int_{-\pi/2}^{\pi/2}\int_0^{\pi} B_r(\sin\theta\cos\phi\cos B_0 + \cos\theta\sin B_0)^2\sin\theta d\theta d\phi, \tag{4}$$

where B_r depends on (θ,ϕ), but B_0 does not. Next, our objective is to expand the binomial factor, $(\sin\theta\cos\phi\cos B_0 + \cos\theta\sin B_0)^2$, and express B_m as the sum of three parts – one proportional to $\cos^2 B_0$, another proportional to $(\sin 2B_0)/2$, and the third proportional to $\sin^2 B_0$.

$$B_m \;=\; (\cos^2 B_0)\,\frac{1}{\pi}\int B_r(\sin\theta\cos\phi)^2 d\Omega \;+\; (\frac{\sin 2B_0}{2})\frac{1}{\pi}\int B_r\sin 2\theta\cos\phi\; d\Omega \;+\; (\sin^2 B_0)\,\frac{1}{\pi}\int B_r\cos^2\theta\; d\Omega, \tag{5}$$

where $d\Omega = \sin\theta d\theta d\phi$ and the integral sign refers to the double integral over θ and ϕ, as indicated in Eq(4).

For the Sun, $|B_0| \le 7.25° \approx 0.126$ radians so that the $\sin^2 B_0$-factor is $\le$0.016, and can be neglected. Likewise, the $\cos^2 B_0$-factor is $\ge$0.984 and can be replaced by 1. Finally, the $(\sin 2B_0)/2$-factor is approximately B_0, which will vary between -0.126 and $+0.126$ during the year. Of course, for a star whose tilt angle is large, we cannot make these approximations, and we may need to keep all three terms.

2.0.2. *Spherical Harmonic Components*

Next, we consider the form of B_r. There are several ways that we could represent this field. One way would be to express B_r as a linear combination of the 'barber pole' eigenfunctions of the flux-transport equation, as DeVore (1987) did in his theoretical analysis of the Sun's large-scale field. This approach might help us to interpret the power spectrum of the mean field in terms of the rigidly rotating patterns that are caused by the latitudinal transport of flux (Sheeley et al. 1987; Wang & Sheeley 1994a; Wang 1998). Another way would be to represent the field in terms of sectors of the form $B_r = f(\theta)\cos m\{\phi - \omega(\theta)t\}$ (where $\omega(\theta)$ is the angular rotation profile), as Sheeley & DeVore (1986a) did in their analysis of the decay of the Sun's mean field. In this paper, I will try a third approach, representing B_r as a linear combination of spherical harmonic components, $Y_l^m(\theta,\phi)$, which are the familiar eigenfunctions of $\nabla^2 B_r = 0$ on the surface of a sphere. (See Eqs (9) and (10) below.) With this understanding,

$$B_r(\theta,\phi,t) \;=\; \sum_{l=0}^{\infty}\sum_{m=-l}^{m=l}\rho_{lm}(t)e^{i\delta_{lm}(t)}Y_l^m(\theta,\phi), \tag{6}$$

where $i = \sqrt{-1}$. Also, ρ_{lm} and δ_{lm} are the amplitude and phase of each harmonic component, Y_l^m, and are defined so that B_r is real. Consequently,

$$B_m \;=\; (\cos^2 B_0)\sum_{l=0}^{\infty}\sum_{m=-l}^{m=l}\rho_{lm}e^{i\delta_{lm}}I_{lm} \;+\; (\frac{\sin 2B_0}{2})\sum_{l=0}^{\infty}\sum_{m=-l}^{m=l}\rho_{lm}e^{i\delta_{lm}}J_{lm} \;+\; (\sin^2 B_0)\sum_{l=0}^{\infty}\sum_{m=-l}^{m=l}\rho_{lm}e^{i\delta_{lm}}K_{lm}, \tag{7}$$

where the coefficients I_{lm}, J_{lm}, and K_{lm} are given by

$$I_{lm} \;=\; \frac{1}{\pi}\int Y_l^m(\theta,\phi)(\sin\theta\cos\phi)^2 d\Omega, \tag{8a}$$

$$J_{lm} \;=\; \frac{1}{\pi}\int Y_l^m(\theta,\phi)\sin 2\theta\cos\phi\; d\Omega, \tag{8b}$$

$$K_{lm} \;=\; \frac{1}{\pi}\int Y_l^m(\theta,\phi)\cos^2\theta\; d\Omega, \tag{8c}$$

and the integral sign refers to the double integral in Eq(4). Thus, I_{lm}, J_{lm}, and K_{lm} (weighted by the respective B_0-dependent factor) are real, and indicate the amounts by which the mean-field 'filter' reduces the amplitude ρ_{lm}

of the field. The spherical harmonic functions, $Y_l^m(\theta,\phi)$, are defined in terms of the Associated Legendre functions $P_l^m(\cos\theta)$, given by Jahnke & Emde (1945), and the normalization factor, N_{lm}, as follows

$$Y_l^m(\theta,\phi) \;=\; N_{lm} P_l^m(\cos\theta) e^{im\phi} \tag{9}$$

$$N_{lm} \;=\; \sqrt{\frac{2l+1}{4\pi}\frac{(l-m)!}{(l+m)!}}. \tag{10}$$

After some algebra, we can rewrite Eqs(8a)-(8c) as

$$I_{lm} \;=\; \frac{N_{lm}}{\pi}\int_{-1}^{1} P_l^m(x)(1-x^2)dx\left[\frac{-4\sin(m\pi/2)}{m(m+2)(m-2)}\right], \tag{11a}$$

$$J_{lm} \;=\; 2\frac{N_{lm}}{\pi}\int_{-1}^{1} P_l^m(x)x(1-x^2)^{1/2}dx\left[\frac{-2\cos(m\pi/2)}{(m+1)(m-1)}\right], \tag{11b}$$

$$K_{lm} \;=\; \frac{N_{lm}}{\pi}\int_{-1}^{1} P_l^m(x)x^2dx\left[\frac{2\sin(m\pi/2)}{m}\right]. \tag{11c}$$

I used standard Mathematica software (Wolfram 1999) to evaluate these expressions and entered the results in Tables 1-3. However, Mathematica defines the Associated Legendre functions using $P_l^m(x) = (-1)^m(1-x^2)^{m/2}d^mP_l(x)/dx^m$, which differ by a factor of $(-1)^m$ from the Jahnke & Emde (1945) values. Therefore, I changed the signs of the odd-m entries in Tables 1-3 to be consistent with the Jahnke & Emde (1945) convention. In retrospect, I could have done this automatically by including an extra factor of $(-1)^m$ in each integrand.

Tables 1 and 3 give non-zero contributions to the Y_0^0 magnetic-monopole component. Ignoring this term, the main contributions to the $\cos^2 B_0$-part of the mean field come from the Y_1^1, Y_2^2, and Y_2^0 components with smaller additional contributions from Y_3^3 and Y_3^1. There are no contributions when $l = 4$ and the higher-order terms are less than 1%. Also, for the Sun, $|B_0| \le 0.126$ and $\cos^2 B_0 \approx 1$, so that the contributions of these harmonics are not weakened appreciably by the B_0-dependence.

However, in Table 2, the main contributions to the $(\sin 2B_0)/2$-part of the mean field are from the Y_1^0 and Y_2^1 components, which are antisymmetric across the equator. These contributions are +0.244 and +0.206, respectively. For small B_0, $(\sin 2B_0)/2 \approx B_0$, which varies annually from -0.126 to +0.126. Consequently, the expected mean-field contributions of the Y_1^0 and Y_2^1 components vary annually and have peak amplitudes of ±3.1% and ±2.6%, respectively. These contributions are comparable to the relatively small, but finite, 3.5% and 2.7% contributions of the Y_3^3 and Y_3^1 components in Table 1. Thus, they ought to be noticeable, especially during sunspot cycles when the polar fields are strong. The other contributions from Table 2 are comparable to the contributions of the higher-order terms in Table 1, which we have already chosen to neglect.

In Table 3, $K_{20} = +0.168$ and $K_{31} = +0.121$. However, these relatively large values can be ignored because the $\sin^2 B_0$ factor (~ 0.016) reduces their net mean-field contributions to less than 1%. Although these entries in Table 3 are unimportant for the Sun, they might contribute appreciably to the mean-field of other stars whose rotation axes may be directed closer to the line of sight. (Of course, for those distant stars, the annual variations induced by Earth's motion around the Sun would be negligible.)

In summary, the Sun-as-a-star field is dominated by the Y_1^1, Y_2^2, and Y_2^0 components of the Sun's field. Also, the mean field has much smaller contributions from the Y_3^3 and Y_3^1 components, and from the Y_1^0 and Y_2^1 components whose strengths are modulated by the annual variation of B_0 as Earth orbits the Sun. Finally, it is important to realize that we have been describing the 'transmission factors' of the mean-field filter and that the real mean field also depends on the amplitude, ρ_{lm}, and phase, δ_{lm}, of the radial field, B_r, that is being filtered. Next, we will use these results to interpret mean-field observations obtained daily at the Wilcox Solar Observatory during the 46-yr interval from May 16, 1975 to the present.

Table 1. Elements of I_{lm} {for the $\cos^2 B_0$-term}

l/m	0	1	2	3	4	5	6	7
0	+0.188							
1	0	+0.173						
2	-0.084	0	+0.103					
3	0	-0.027	0	+0.035				
4	0	0	0	0	0			
5	0	-0.003	0	+0.004	0	-0.005		
6	0	0	0	0	0	0	0	
7	0	-0.001	0	+0.001	0	-0.001	0	+0.002

Table 2. Elements of J_{lm} {for the $(\sin 2B_0)/2$-term}

l/m	0	1	2	3	4	5	6	7
0	0							
1	+0.244	0						
2	0	+0.206	0					
3	-0.093	0	+0.085	0				
4	0	0	0	0	0			
5	-0.018	0	+0.018	0	-0.015	0		
6	0	0	0	0	0	0	0	
7	-0.007	0	+0.007	0	-0.007	0	+0.006	0

Table 3. Elements of K_{lm} {for the $\sin^2 B_0$-term}

l/m	0	1	2	3	4	5	6	7
0	+0.188							
1	0	+0.086						
2	+0.168	0	0					
3	0	+0.121	0	-0.017				
4	0	0	0	0	0			
5	0	+0.045	0	-0.034	0	+0.007		
6	0	0	0	0	0	0	0	
7	0	+0.026	0	-0.023	0	+0.017	0	-0.004

3. SUN-AS-A-STAR MAGNETIC FIELD MEASUREMENTS FROM WSO

3.1. *27-day rotational modulation*

Figure 1 shows daily measurements of the Sun's mean field obtained at WSO since 16 May 1975. Approximately 17,000 points over 46 years give a blurred distribution with peaks and valleys around sunspot maximum and minimum

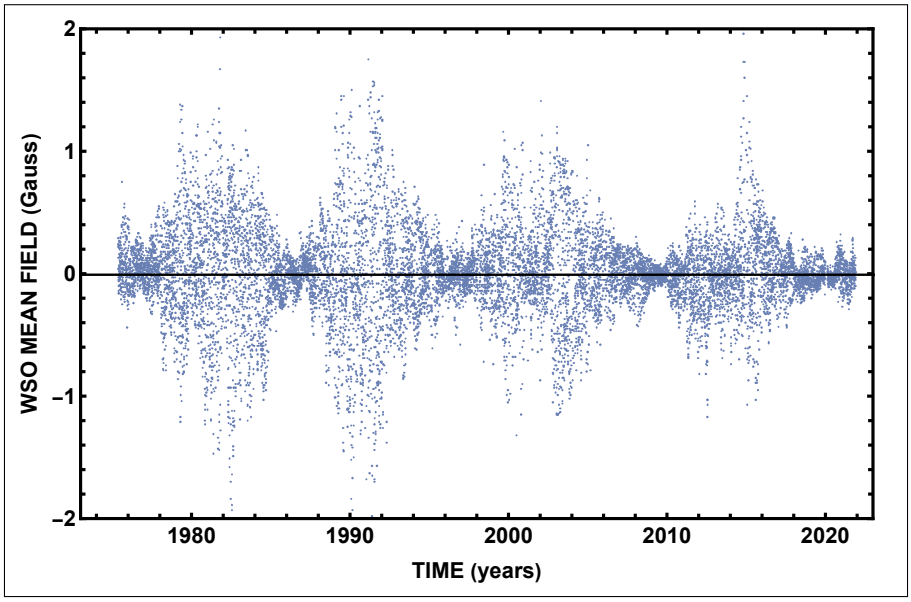

Figure 1. Daily measurements of the Sun's mean line-of-sight field obtained at WSO from 16 May 1975 to 16 November 2021. The blurred cloud of points shows peaks of strength $\gtrsim$1G in each cycle, and valleys of strength $\lesssim$0.2G near sunspot minimum.

in each of four sunspot cycles. This figure is essentially the same as the one that is shown on the WSO web site (http://wso.stanford.edu), and leaves us with the question of how to extract information from these data. A big clue is contained in a plot of the data obtained during the first year of observations, as shown in Figure 2. The field oscillates with a period of about 27 days ($\sim$0.074 yr), before degrading toward the end of the year, as the corresponding

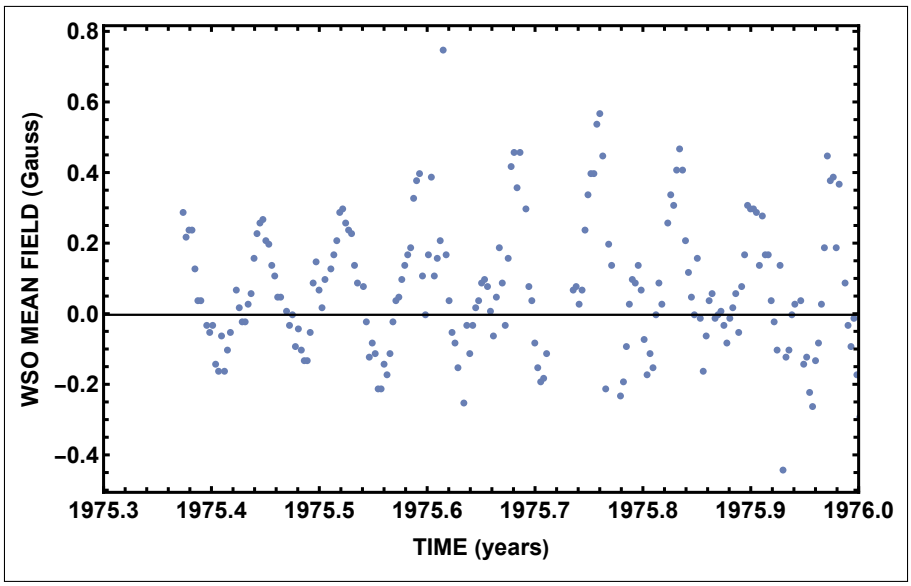

Figure 2. Mean-field measurements during the first year of observations at WSO, showing the end of a 27-day recurrence pattern, that was associated with the gradual demise of a long-lived coronal hole.

low-latitude coronal hole gradually died (Sheeley et al. 1976). What we would like to know is how much power is contained in this 27-day modulation and how that power varies with time during the 46-yr interval. In effect, we are asking for the envelope of this mean-field time series.

There are several approximately equivalent ways to produce this envelope. One way is to divide the time base into 27-day segments and to compute the maximum-minimum difference of the mean-field values on each segment. By plotting the absolute values of these differences, we would obtain a display of the mean field variation similar to the one that Sheeley & Wang (2015) obtained in their paper describing the rejuvenation of the Sun's large-scale magnetic field. A similar result is obtained by computing the standard deviation of the mean field on each 27-day segment (allowing for data gaps when taking the averages), and then plotting that value as a function of time. Another, nearly equivalent procedure is to set the mean-field data gaps equal to zero before computing the standard deviations, and then to perform a 27-day moving average of those standard deviations. This is the approach that I shall use in the remainder of this paper.

Figure 3 shows this 27-day moving average, compared with the monthly averaged sunspot number (divided by 2000) during cycles 21 - 24. As described previously using the 'max-min' display (Sheeley & Wang 2015), the mean field originates in episodic bursts whose amplitudes often tend to be large as the sunspot cycle enters its declining phase. Also, one can see the decrease of the mean field strength during 1976 as the sunspot number reached its 11-year minimum and the low-latitude coronal hole died (*cf.* Figure 2). Finally, note that the amplitudes of the peaks in Figure 3 are about 1.4 times smaller than those in Figure 1. This is close to the $\sqrt{2}$ that one might expect for the difference between the standard deviation and the envelope of a curve. (For example, if $f(t) = A(t)cos\omega t$, the envelope is $\pm A(t)$ and the standard deviation is $A(t)/\sqrt{2}$.)

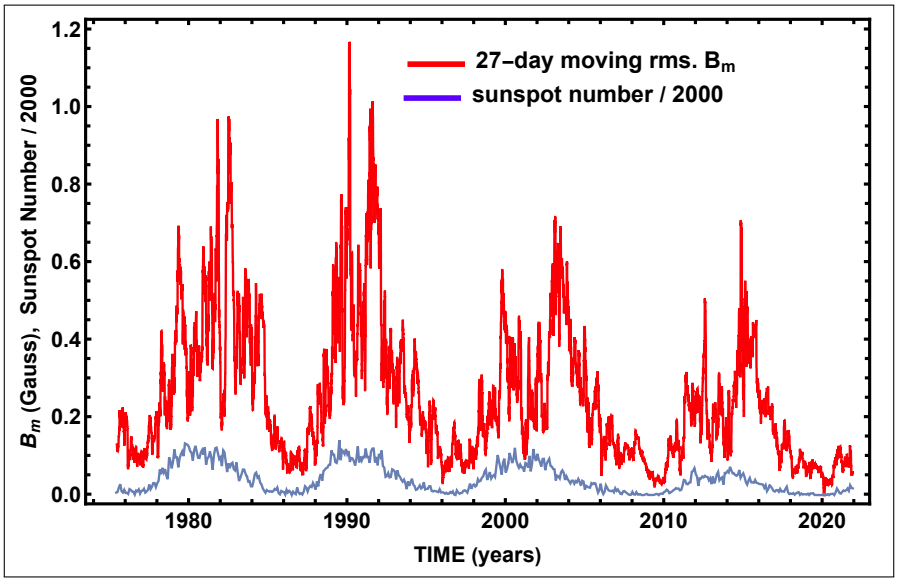

Figure 3. Root-mean-square deviation of the WSO mean field from its 27-day average value (red), compared with the monthly averaged sunspot number from the Royal Observatory of Belgium (SILSO) divided by 2000 (blue) during cycles 21 - 24. This comparison shows the tendency of the mean field to occur in episodic bursts, often when the sunspot cycle begins its decline.

3.2. *Using the Fourier transform approach*

Next, we return to the WSO mean-field measurements that we displayed as a function of time in Figure 1. After setting the missing field strengths equal to 0, we take the discrete Fourier transform defined by

$$f_s = \frac{1}{\sqrt{N}} \sum_{k=1}^{N} B_k e^{2\pi i(k-1)(s-1)/N} \tag{12}$$

where B_k refers to the individual mean-field measurements whose index, k, runs from 1 to $N = 16,987$, corresponding to the most recent measurement on 16 November 2021. In this case, the frequency, ω, in rad day^{-1} is given by

$$\omega = 2\pi s/N. \tag{13}$$

Because f_s is a complex number, one typically plots the power, $P(\omega)$, defined as the positive number, $f_s^* f_s$, versus ω. However, to keep the units in Gauss, I plot the positive square root of this power. Also, it is not necessary to include the full range $(0, 2\pi)$ because the spectrum is symmetric about the point $\omega = \pi$. Moreover, we do not even need to include all of the half range $(0, \pi)$ because the lines disappear after the $m = 3$ peak around $\omega = 0.7$ rad day^{-1}. This is consistent with our expectations from Table 1, which gives 0 for $m = 4$, and less than 1% for $m = 5$.

The power spectrum in Figure 4 shows three main peaks at frequencies of approximately $\omega = 0.231$, 0.460, and 0.702 rad day^{-1}. These frequencies are in the ratio of approximately 1:2:3, corresponding to a fundamental rotation rate with $m = 1$ and its first two harmonics with $m = 2$ and $m = 3$. The associated periods are approximately 27.2, 13.6,

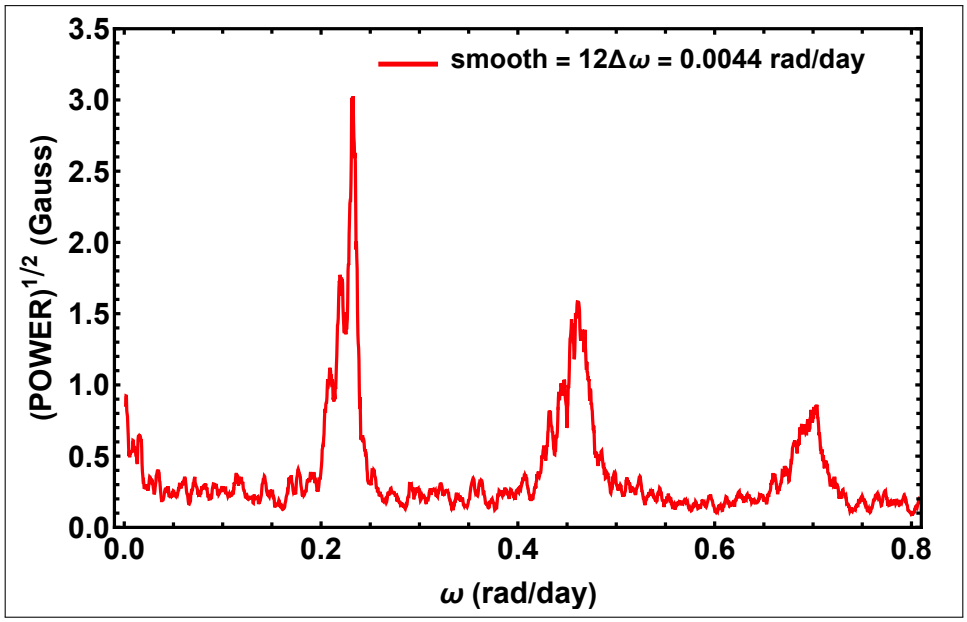

Figure 4. Power spectrum of daily WSO mean-field measurements during 1975 - 2021, showing three main sectorial peaks at $\omega \approx 0.231$, 0.460, and 0.702 rad day^{-1} (corresponding to a rotation period of 27.2 days and its second and third harmonics). The plot has been smoothed in a moving average of 12 resolution elements, each of size $\Delta\omega = 2\pi/N = 3.70\times10^{-4}$ rad day^{-1}.

and 9.0 days, respectively. Evidently, we are seeing rigidly rotating recurrence patterns of two-sector, four-sector, and six-sector fields (*i.e.* the dipole, quadrupole, and hexapole fields).

These regions are shown separately in the three panels of Figure 5. Each spectrum is displayed with the same 12 unit smoothing, which is 12 times the $2\pi/N$ resolution for $N\sim$ 16,987 points, and corresponds to 0.0044 rad day^{-1}. On the

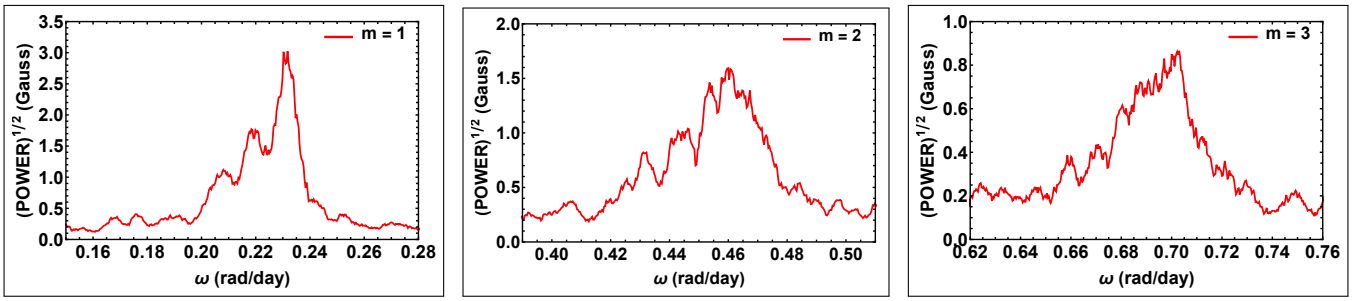

Figure 5. Segments of the power spectrum in Figure 4, showing the fine structure of the $m = 1$ (left), $m = 2$ (middle), and $m = 3$ (right) components for the full time interval 1975 - 2021.

low-frequency side of the fundamental peak at $\omega = 0.231$ rad day^{-1}, there are peaks at 0.219 and 0.208 rad day^{-1}, corresponding to periods of approximately 28.7 and 30.2 days, respectively. The 28.7-day period is comparable to the ∼28.5-day recurrence period of the slanted patterns seen around sunspot maximum in Bartels displays of the interplanetary magnetic field observed by in-ecliptic spacecraft and inferred from Earth-based magnetometers (Svalgaard

& Wilcox 1975; Hoeksema 1984; Sheeley et al. 1985; Sheeley & DeVore 1986b; Wang & Sheeley 1994b). However, the 30.2-day peak has no in-ecliptic counterpart, and therefore probably originates in rigidly rotating structures at latitudes that are beyond the reach of the in-ecliptic measurements, as discussed in Section 3.2.1 below.

Although the frequencies of the main peaks of the $m = 1$, $m = 2$, and $m = 3$ distributions occur in the ratio of 1:2:3, the frequencies of the sidebands do not occur in this ratio. In particular, the $m = 2$ and $m = 3$ sidebands are not 'blurred out' harmonics of the peaks at 0.208 and 0.219 rad day^{-1}. Not only do the $m = 2$ structures occur at different frequencies than we would expect for second harmonics, but also these structures are accompanied by additional features for which there is no corresponding peak in the sidebands of $m = 1$. For $m = 3$, there are even more fluctuations, crowding into a broad slope of nearly continuous intensity.

Finally, we note in Figure 4 that there is a noisy 'ledge' of strength ∼0.6 G at $\omega \sim 0.017$ rad day^{-1}. This structure corresponds to a weak annual variation associated with the motion of the Earth around the Sun. As discussed in Section 2, this annual variation is introduced through B_0 - Earth's latitude in the Sun's polar coordinate system. At even lower frequencies, the spectrum rises steeply, and the expected peak at $\omega \approx 0.0016$ rad day^{-1} (corresponding to the 11-yr sunspot cycle) is not visible in this 0.0044 rad day^{-1} smoothed plot. Kotov (2019) has used mean-field observations since 1968 to study this annular variation in greater detail.

3.2.1. *The temporal origin of the peaks in the power spectrum*

The next problem is to find the temporal origin of these spectral peaks. We do this by selecting the frequency range of interest and then taking the inverse Fourier transform through that spectral window. We use the inverse transform

$$B_k = \frac{1}{\sqrt{N}} \sum_{s=1}^{N} f_s e^{-2\pi i(k-1)(s-1)/N}, \tag{14}$$

but with f_s multiplied by a function of s (or equivalently ω) that is 1 on the interval of interest and 0 elsewhere. Note that f_s is the original complex Fourier transform given by Eq(12), and not the absolute value that was used in Figure 4. In general, the inverse Fourier transform is also a complex number, so we calculate the standard deviation, σ, from the relation $\sigma^2 = < |B_k|^2 > - | < B_k > |^2$, where in the second term, we compute the 27-day average of B_k before we take its absolute value and square it. In this case, it is easy to show that $\sigma^2 = \sigma_r^2 + \sigma_i^2$ (*i.e.* the standard deviation of B_k is the square root of the sum of the squares of the standard deviations of its real and imaginary parts).

Figure 6 was created by selecting a disjoint interval consisting of the three principal peaks of the power spectrum -

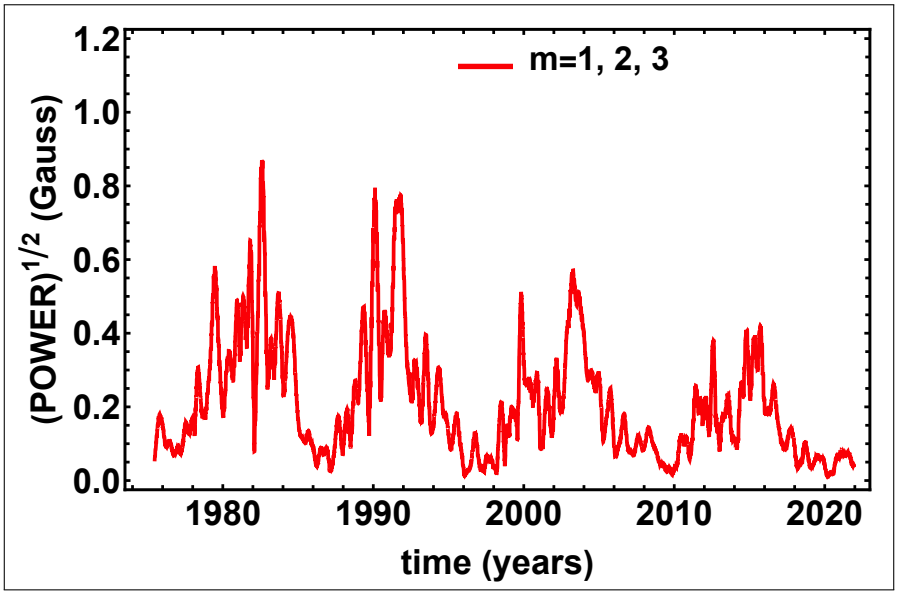

Figure 6. Result of inverting the Fourier transform of the mean field back to the temporal domain using all three frequency windows (0.20-0.25), (0.42-0.50), and (0.65-0.73) rad day^{-1} (corresponding to the $m = 1$, $m = 2$, and $m = 3$ sectoral modes, respectively), and then displaying the 27-day moving standard deviation of this inverted transform.

specifically, (0.20-0.25), (0.42-0.50), and (0.65-0.73) rad day^{-1} - and then by displaying the root-mean-square power in the inverse transform. This plot is essentially the same as Figure 3 without the noise. Because we have not included power at the frequency of the annual variation (0.0172 rad day^{-1}), we have removed potential contributions from Table 2, so that the only contributions come from modes in Table 1. This leaves only the Y_1^1 (and possibly the Y_3^1) components as likely contributors from the $m = 1$ sector, and only the Y_2^2 and Y_3^3 components as contributors from the $m = 2$ and $m = 3$ sectors, respectively. So, the red curve in Figure 6 indicates contributions from the horizontal dipole, quadrupole, and hexapole components (Y_1^1, Y_2^2, and Y_3^3), and possibly a small contribution from Y_3^1.

Next, we ask how this non-axisymmetric power is distributed among the $m = 1$, $m = 2$, and $m = 3$ sectorial modes. For this purpose, we use the individual frequency ranges (0.20-0.25), (0.42-0.50), and (0.65-0.73) rad day^{-1}, which correspond to the fundamental, second, and third harmonics shown in Figures 4 and 5. The 27-day running averages are shown in Figure 7. In general, the $m = 1$ component contributes the most and the $m = 3$ component contributes the least. With a few exceptions, the mean-field is dominated by the $m = 1$ and $m = 2$ sectoral modes. The $m = 1$ component has large peaks in 1982, 1991, 2003, and a small one in 2015 that we recall from a nearly identical plot of the equatorial dipole, that was derived from spatially resolved WSO observations (Sheeley & Wang 2015). Also, the $m = 2$ component has moderately large, but narrow, peaks in 1981, 2000, and 2012. The $m = 3$ component has a large, narrow peak in 1991 when the $m = 1$-2 values are temporarily low. Also, in the relatively weak sunspot cycle 24, the three components have nearly coincident peaks of approximately equal strength, which combine to give a stronger peak of total mean-field power, as seen in Figure 6.

Based on the factors in Tables 1 and 2, we expect that the $m = 1$ power originates primarily from the Y_1^1 horizontal dipole component of field and secondarily from the Y_3^1 component. As mentioned above, by filtering out annual variations, we have excluded contributions from the Y_2^1 component, that would otherwise occur through the B_0 factor. Likewise, the Y_3^2 component is excluded from the $m = 2$ sector, which indicates power in the Y_2^2 component alone.

Finally, we have the impression in Figure 7 that the temporal fluctuations become systematically finer as m increases from 1 to 3. This is consistent with the increased coarseness of the power spectra in Figures 4 and 5 as m increases: For $m = 1$, the peaks were often resolvable; for $m = 2$, they formed coarser structures; and for $m = 3$, they merged into a 'bumpy' continuum. In a previous analytical study of the mean field, we noted that the field depended on the product mt, not on m and t separately. This meant that the mean field would decay as $1/m$ in the absence of meridional flow (Sheeley & DeVore 1986a). In particular, a 4-sector field would decay twice as fast as a 2-sector field, and a 6-sector field would decay three times as fast. When flow was present, this analytical simplification did not occur. However, the apparent trend in Figure 7 indicates that a monotonic relation may still be present.

Next, we look for the origins of the three $m = 1$ peaks at $\omega = 0.231$, 0.219, and 0.208 rad day^{-1}, shown in the left panel of Figure 5. To do this, we select relatively narrow spectral windows surrounding these peaks, and then invert the Fourier transform and plot the running 27-day rms averages. For the intervals, $\omega = 0.226 - 0.237$, $\omega = 0.215 - 0.225$ and $\omega = 0.198 - 0.212$ rad day^{-1}, we obtain the blue curves in Figure 8. Here, the red curve indicates the total $m = 1$ power from the top panel of Figure 7. So we are comparing the temporal origin of the individual $m = 1$ peaks with the temporal origin of the combined $m = 1$ power.

Like Fourier transforms of continuous functions, these Fourier transforms of discrete functions have peaks whose widths, $\Delta\omega$, are inversely related to the lifetimes, Δt, of the corresponding temporal structures. In fact, $\Delta\omega\Delta t \sim 8$ for full widths at e^{-1} maximum and $\Delta\omega\Delta t \sim 8\ ln2 \approx 5.54$ for full widths at half maximum. Consequently, the narrow $m = 1$ peaks with $\Delta\omega \sim 0.01$ rad day^{-1} in the left panel of Figure 5 correspond to long-lived features with $\Delta t \sim 1 - 2$ yrs.

In the top panel of Figure 8 the blue curve refers to the power in the spectral 'line' at $\omega = 0.231$ rad day^{-1} (corresponding to a period of approximately 27.2 days). This blue curve tends to follow the more rapidly fluctuating red curve, with appreciable contributions during each of the four sunspot cycles. Thus, most of the two-sector power originates in long-lived features that recur with a period of 27.2 days, and presumably corresponds to quasi-vertical patterns in the 27.27-day Carrington stackplots of mean-field observations.

In the middle panel, the blue curve refers to power in the spectral line at $\omega = 0.219$ rad day^{-1} (28.7days). Most of the 28.7-day power originates in 1979-1985 and 1989-1993 coincident with large peaks of 27-day power. This overlapping trend did not continue into sunspot cycles 23 and 24 when the 28.7-day power was much smaller. This suggests that ∼28.5-day stackplot patterns may have been weaker or less frequent in cycles 23 and 24 than in cycles 21 and 22.

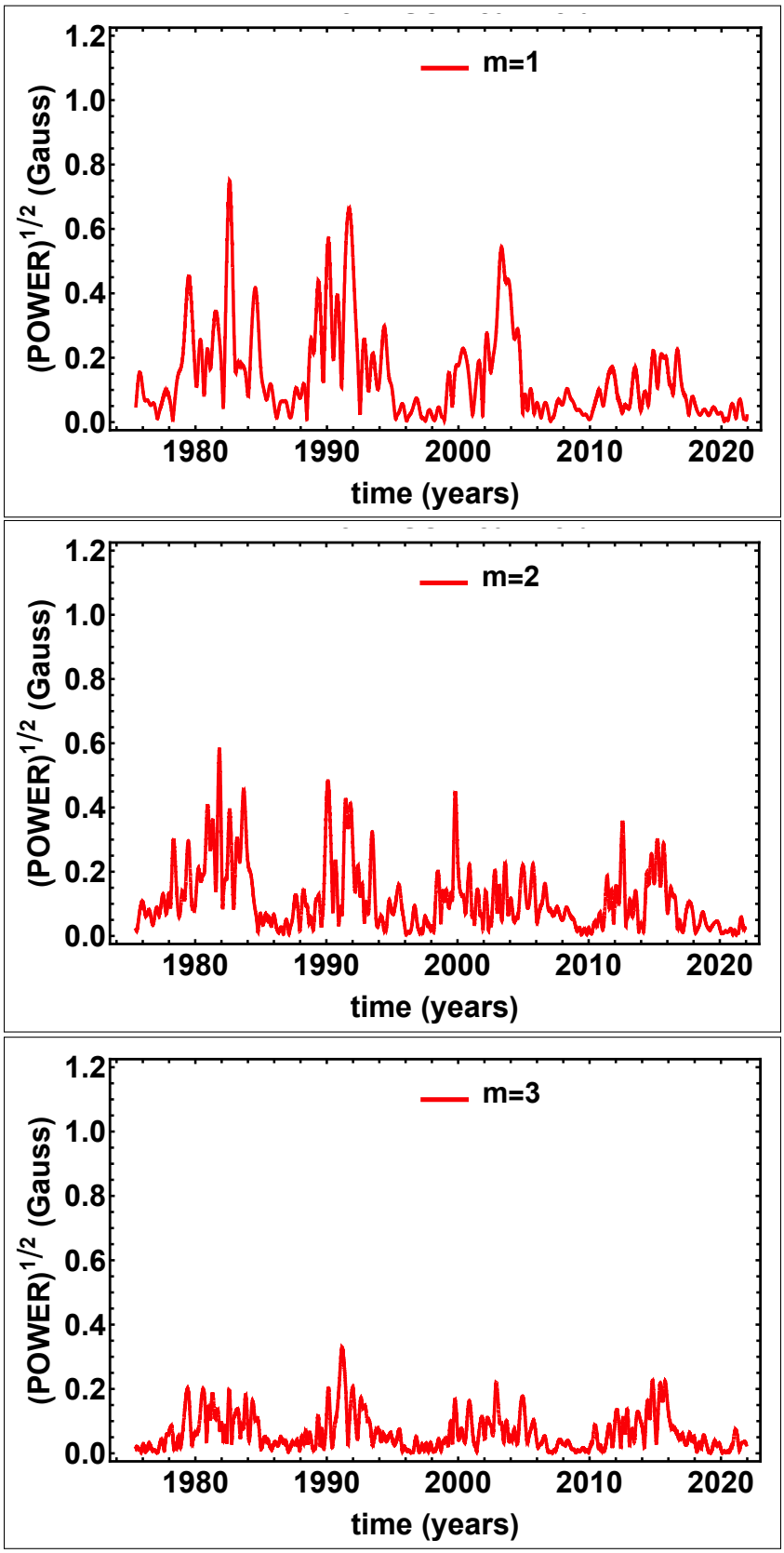

Figure 7. Power in the two-sector (top), four-sector (middle), and six-sector (bottom) patterns of the mean field. Referring to Table 1, we expect this power to originate mainly in the Y_1^1, Y_2^2, and Y_3^3 components of the field.

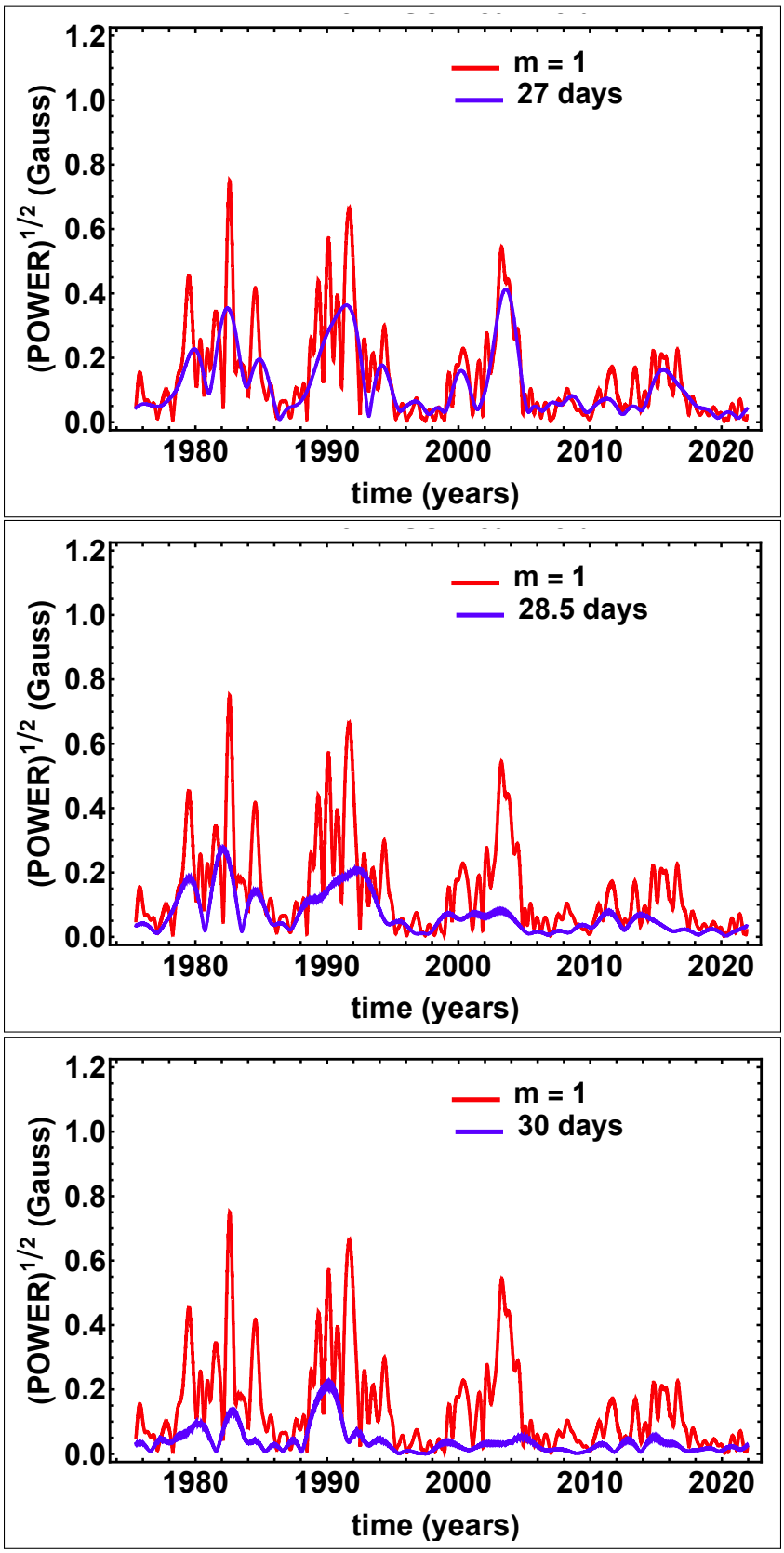

Figure 8. Two-sector ($m = 1$) power from 27-day (top), 28.5-day (middle), and 30-day (bottom) structures (blue) compared with their total $m = 1$ power (red). This figure shows that 27-day power originates in all four sunspot cycles, but the 28.5-day and 30-day power come mainly from the stronger sunspot cycles 21 and 22.

In the bottom panel, the blue curve indicates power in the spectral line at $\omega = 0.208$ rad day^{-1} (30.2 days). Most of this ∼30-day power occurred in 1989-1990, with lesser amounts during 1980 and 1982-1983, and only trace amounts in sunspot cycles 23 and 24.

To summarize the results of Figure 8, the power depends on the rotation period with 27-day power coming from all four sunspot cycles (but with a relatively small contribution from the weakest sunspot cycle 24). The 28.5-day power originates mainly in sunspot cycles 21 and 22 with very small contributions from cycles 23 and 24. The 30-day power comes mainly from the year 1989 in cycle 22 and secondarily from small peaks in cycle 21.

The lack of substantial 30-day power after 1990 provides another way to isolate the power during 1989 - 1990. We simply move the starting point of the Fourier transform backwards in time through the year 1989 and watch the height of the 30-day peak increase. Figure 9 shows a sample of the power spectra obtained by moving the starting time backward from 02 February 1990 (CR1826) in steps of 3 Carrington rotations (approximately 82 days) to 09 January 1989 (CR1811). During this sequence, the 30-day (0.208 rad day^{-1}) peak emerges from a continuum level at about 0.5

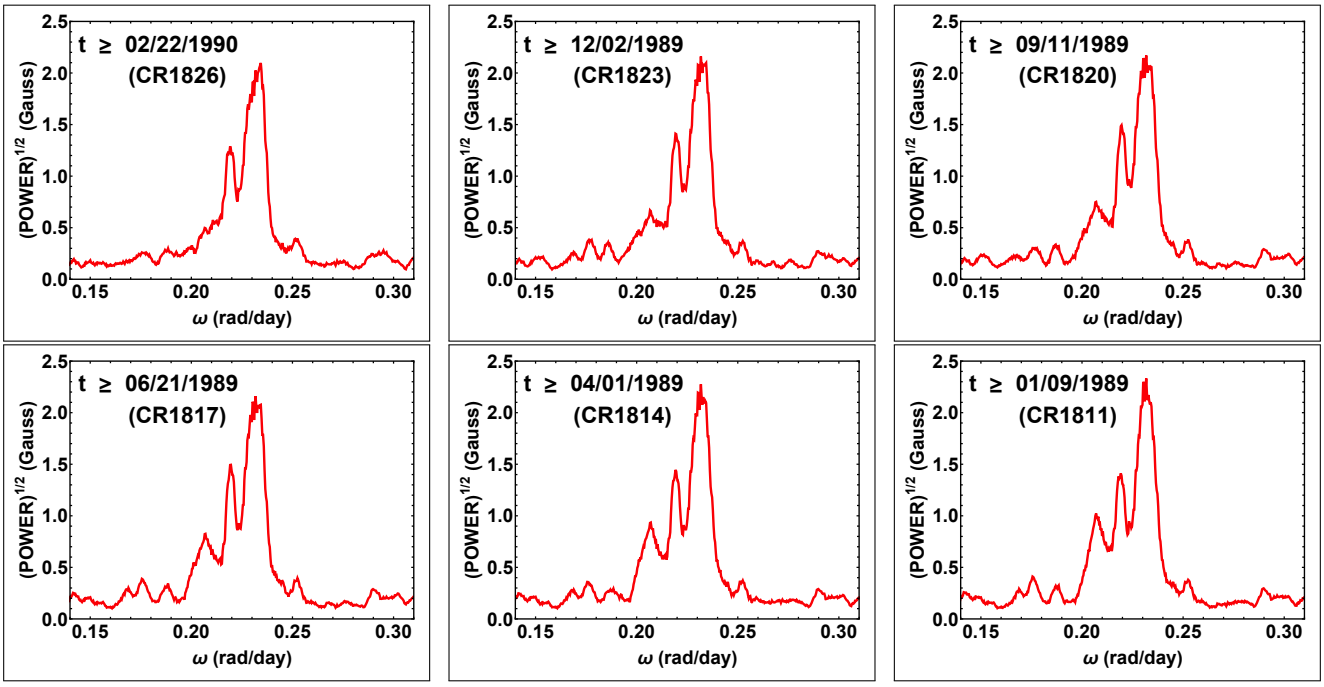

Figure 9. Power spectra of WSO mean-field measurements from time, t, to the end of the data set on 16 November 2021, showing the emergence of the ∼30-day (0.208 rad day^{-1}) peak as t decreases from 22 February 1990 to 09 January 1989.

G to a maximum height of about 1.0 G. Although not shown here, a movie with 1-rotation time resolution indicated that the 30-day peak emerged from the continuum at CR1824 (29 December 1989) and strengthened until it reached about 1.0 G at CR1811 (09 January 1989), corresponding to a lifetime of 13 rotations (1 yr and 11 days). Thus, the 30-day oscillation spanned the 1-year interval from 1989 to 1990.

We can continue this approach by moving the starting point of the Fourier transform forward in time to successively exclude major contributions to the 30-day, 28.5-day, and 27-day periods. Referring to Figure 8, we select the first starting time on 09 January 1989 when substantial power remained in all three rotational periods. This is shown in the upper-left panel of Figure 10. Then, we move farther in time to 01 June 1991, which is well after the peak of 30-day power, but still includes power at 28.5 days and 27-days, as shown in the upper-right panel of Figure 10. Next, we choose 17 January 1996, which is after the large peak of 28.5-day power. However, 17 January 1996 is still before the occurrence of the large peak of 27-day power in 2003-2004, and this contribution is shown in the lower-left panel of Figure 10. Finally, we select 02 January 2005 to remove this large peak of 27-day power. The remaining 27-day power comes from a small peak in 2015 -2016, as shown in the lower-right panel of Figure 10. This contribution seemed very important when it rejuvenated the large-scale field in sunspot cycle 24 (Sheeley & Wang 2015). In the next section, we shall compare these observations with spatially resolved magnetograms and find that the peaks of 27-day power

tend to occur toward the end of sunspot maximum when the sunspot belts are closer together and allow large unipolar magnetic regions to form at the equator.

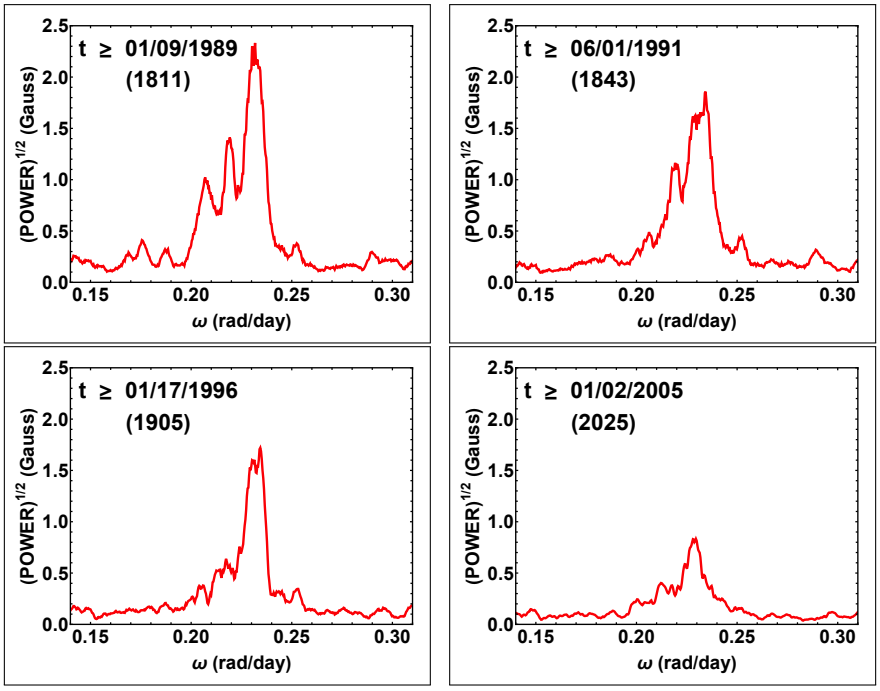

Figure 10. Power spectra of the mean field, showing the $m = 1$ fine structures at 0.21, 0.22 and 0.23 rad day^{-1} as the starting time, t, of the Fourier transform is increased. The 30-day and 28.5-day sidebands are successively reduced as t shifts from 1989 to 1991 and then to 1996. The 27-day peak is reduced when t shifts to 2005, leaving a small contribution from 2015 - 2016.

3.2.2. *Corresponding solar images*

Next, we look for these magnetic patterns in spatially resolved solar observations. We begin with Figure 11, which shows Carrington maps of the photospheric magnetic field obtained at the National Solar Observatory (NSO)[2]. At NSO, each of these maps was divided by $\mu = \sin\theta\cos\phi$ to convert the observed line-of-sight component to a radial component, assuming that the fields are radial at the photosphere where they are measured. Thus, we regard these maps as displays of the radial component of photospheric field.

This figure contains images from the start of sunspot maximum (left column) and the end of sunspot maximum (right column) in sunspot cycles 21 (top row), 22 (middle row), and 23 (bottom row). In the left panels, each sunspot cycle has progressed far enough that several large active regions have emerged to form activity belts with flux streaming poleward and eastward (leftward) from those belts. However, the sunspot cycles have not progressed far enough for flux to spread equatorward to fill in the wide gaps between the two belts, as has happened at the times of the images in the right panels. In fact, by the end of the sunspot-maximum era, the two activity belts have reached sufficiently low latitudes and narrow separations that the equatorward diffusion of flux dominates the poleward convection by meridional flow, causing flux to accumulate around the equator.

We have encountered these phenomena before. First, in numerical simulations of the mean field, Sheeley & DeVore (1986b) found that the 28-29-day recurrent patterns originated in flux that was migrating poleward from its sources in the sunspot belts. The dramatic eastward drift of these patterns is well known to many of us from viewing time-lapse movies of Carrington maps like the ones in Figure 11. Second, Sheeley & Wang (2015) found that a juxtaposition of northern-hemisphere and southern-hemisphere active regions during the second half of 2014 created a large region of positive-polarity flux at the equator, which produced a major rejuvenation of the Sun's large scale field. As shown in the top panel of Figure 8, the 27-day power in the two-sector component of the mean field reached a peak at this time.

[2] https://nispdata.nso.edu/ftp/kpvt/synoptic/mag

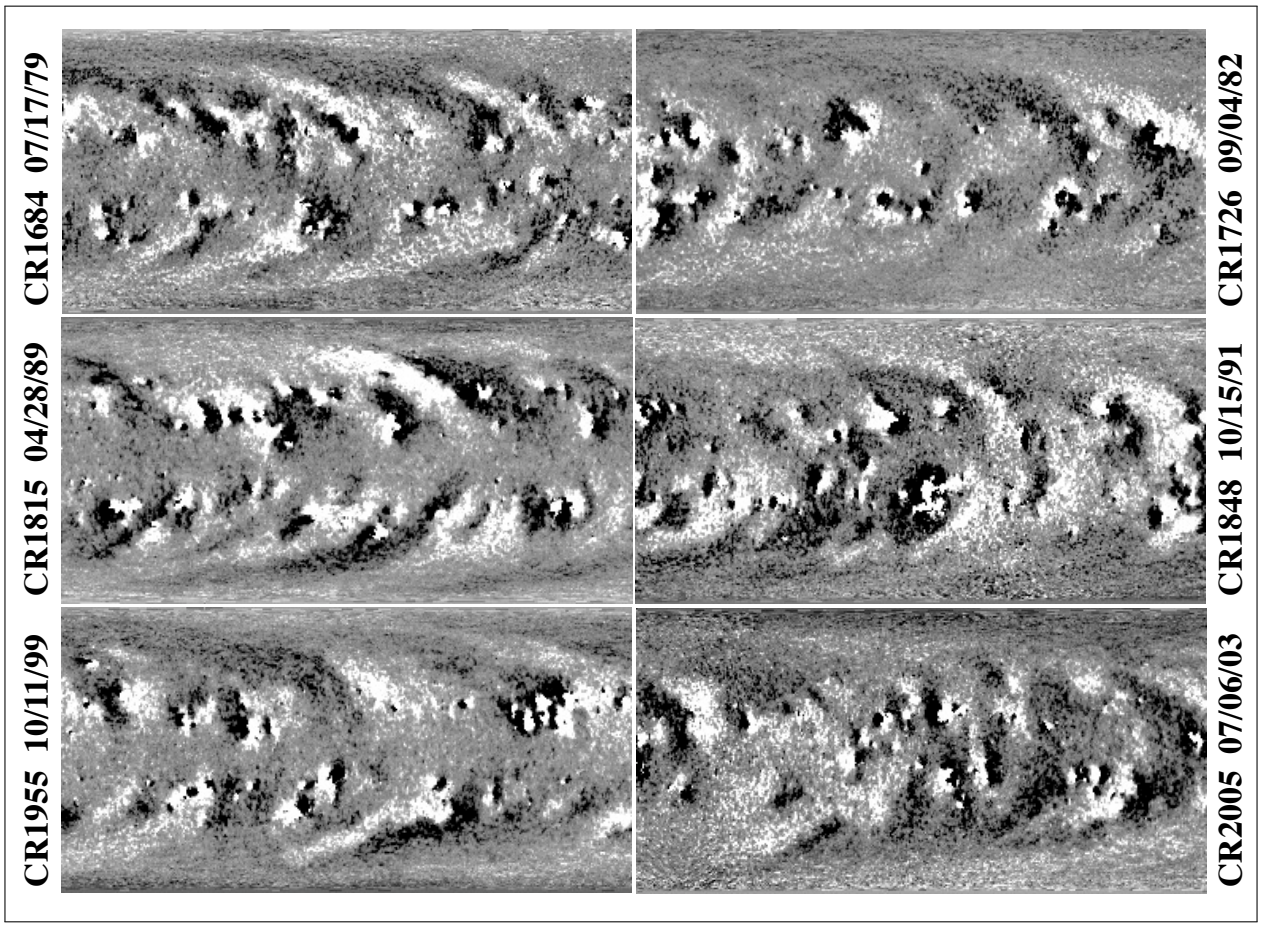

Figure 11. NSO Carrington maps of the radial magnetic field during sunspot cycles 21 - 23 (top, middle, and bottom panels, respectively), showing flux streaming poleward and eastward from the sunspot belts during the initial phase of sunspot maximum (left panels) and flux accumulating in the equatorial region between the sunspot belts at the end phase of sunspot maximum (right panels). Longitude runs left to right from 0° to 360°, and sine latitude ranges from -1 to +1 from bottom to top of each map. Positive polarity is white and negative is black. Dates refer to the starting times at the right edge of each map.

Also, Sheeley & Wang (2015) noted that this rejuvenation of the large-scale field was not an isolated characteristic of sunspot cycle 24, and that similar enhancements of the equatorial dipole field in 1982, 1991, and 2003 have marked the end of the sunspot maximum era (or the start of the declining phase) of cycles 21, 22, and 23.

Another reason for selecting the images in Figure 11 was to relate these flux distributions to the profiles of spectral power, especially for the two-sector ($m = 1$) plots in Figure 8. Thus, the maps in the top panel of Figure 11 occur in 1979 and 1982 when there were peaks in the spectra for 27 days, 28.5 days and, to a lesser extent, 30 days. The maps in the middle panels occurred in 1989 when the 30-day power reached its maximum, and in 1991 when the 27-day and 28.5-day power reached their maximum values. The map in the bottom-right panel was chosen because it occurred in 2003 when the 27-day power dominated the two-sector spectrum. As one can see, it shows a large two-sector pattern of equatorial flux with positive-polarity flux left of center and negative-polarity flux right of center.

In choosing these images, I looked for strong poleward streams in each sunspot cycle. However, I did not always find them. Whereas the maps in the upper-left and middle-left panels show major streams, the map in the lower-left panel (CR1955, 11 October 1999) shows relatively weak streams, despite the fact that it was at the same phase of the sunspot cycle. Those 1999 streams are only slightly more impressive than the weak streams in 1982, 1991, and 2003 in the right column. This favoring of sunspot cycles 21 and 22 over cycle 23 is consistent with the power spectra in Figure 8, which show more 28.5-day and 30-day power during cycles 21 and 22 than during cycle 23.

If the 28.5-day power originates in poleward migrating flux from large active regions, as previously reported (Sheeley & DeVore 1986b), then it seems plausible that the much rarer 30-day power in 1989 is a statistical fluctuation caused

by the emergence of an especially large, high-latitude active region at that time. The strong, northern-hemisphere stream in the middle-left panel of Figure 11 originated in such an active region.

The right panel of Figure 12 shows the evolution of this region during CR1811-1818 (09 January 1989 - 19 July 1989) when sunspot cycle 22 reached the start of its 3-4 years of high sunspot activity[3]. Each image is the northern-hemisphere part of a Carrington map that has been cropped at the equator. Thus, longitude runs left to right from 0° to 360° and sine latitude runs bottom to top from 0 to +1. The faint, yellow lines provide a reference drift for a 30.2-day rotation, corresponding to the frequency $\omega = 0.208$ rad day^{-1} that we obtained from the power spectra in Figures 4 and 5.

For comparison, the left panel of Figure 12 shows the evolution of a much smaller region during CR1788-1795 (22 April - 30 October 1987) at the start of cycle 22. Both regions emerged at latitudes ∼35°, and their fluxes evolved into

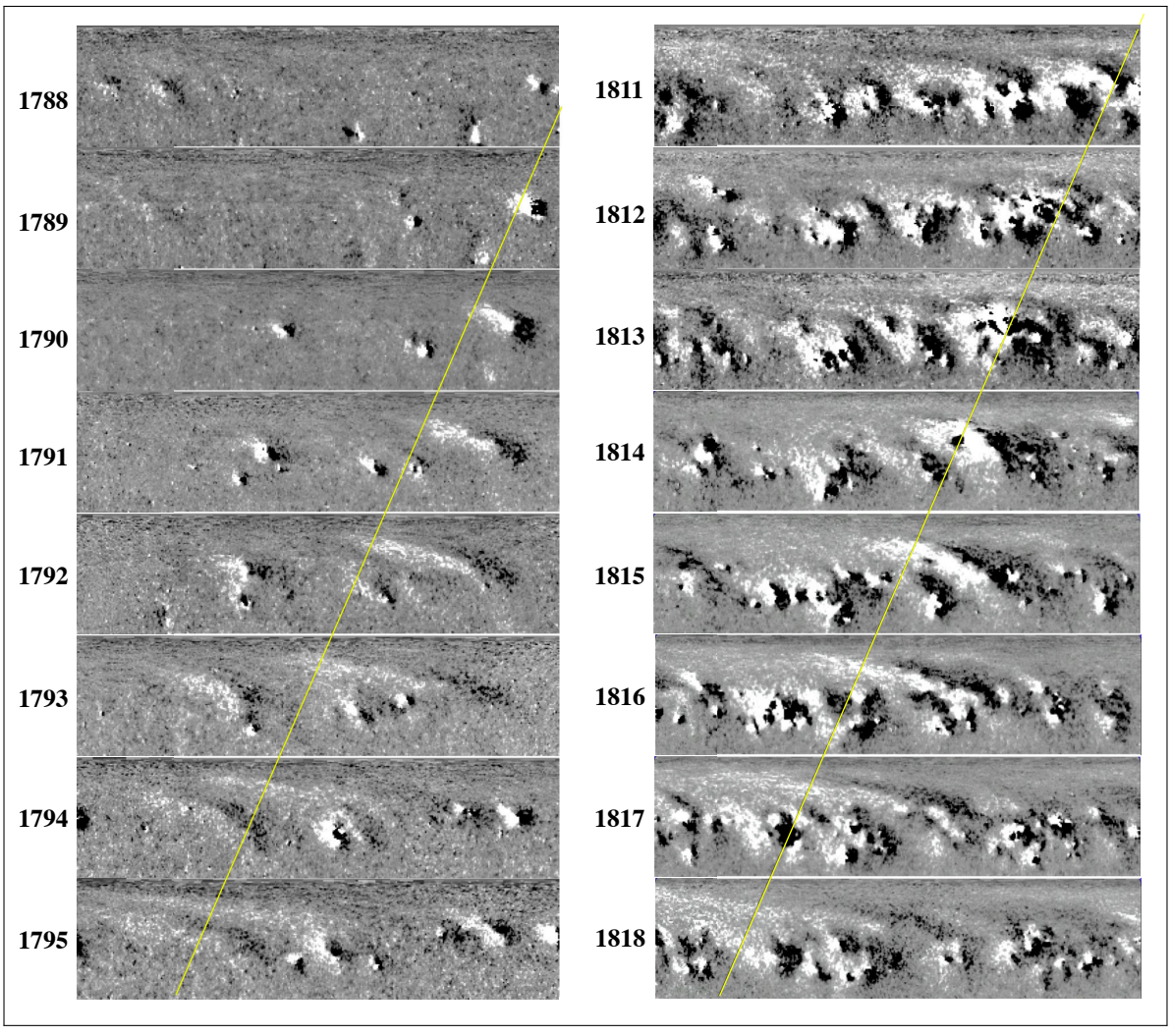

Figure 12. Carrington maps, cropped to show northern-hemisphere magnetic fields as a function of longitude (0° to 360° on the horizontal axis) and sine latitude (0 to +1 on the vertical axis). (left): CR1788-1795 (22 April - 30 October 1987), showing the northward and eastward drift of flux from a new-cycle active region. (right): CR1811-1818 (09 January - 19 July 1989), showing a stronger stream from a bigger active region near sunspot maximum. Faint yellow lines indicate a 30.2-day rotation.

similar patterns at comparable speeds. (An interesting, and probably coincidental, similarity is that both streams were replenished by flux from a second active region that emerged 3-4 rotations later toward the left side of each panel.)

[3] J.W. Harvey recently reminded me that during CR1813, this region (5395) was the source of many X-ray flares and coronal mass ejections (CMEs), two of which were responsible for the blackout of the Hydro-Québec power system on 13 March 1989 (Boteler 2019).

The major difference is that the 1989 source was larger and stronger than the 1987 source. Presumably, this difference in strength was responsible for the difference in spectral power shown in Figure 8. The 1989 stream coincided with a large peak of 30-day spectral power, whereas the 1987 stream did not.

At the ∼35° latitude of these two active regions, the rotation period of small-scale magnetic tracers is about 29 days (Snodgrass 1983). However, within a few Carrington rotations, these streams of trailing, positive-polarity flux had drifted poleward into the 45° latitude range where the rotation period is 30 days. Although one can confirm this by measuring the vertical locations of the streams in these images, one can also refer to the faint yellow lines, which provide a 30.2-day reference drift. These lines track the trailing streams of positive-polarity flux fairly well until the tails of the streams reach latitudes above 45° and also begin to merge with flux from other active regions.

Multi-latitude stackplots of the WSO-derived source-surface field support the identification of the 1989 pattern as the source of the 30-day power (Wang & Sheeley 1994b). Calculated for 1977 - 1993, these stackplots show a rare, 30-day, two-sector recurrence pattern over a wide range of latitudes from 20°N to 80°N during 1989. It is the most prominent 30-day pattern during that 16-year interval. In addition, its positive-polarity sector moves from right to left across the Carrington frame during 1989, so that the phase of this two-sector pattern also agrees with that of the field in Figure 12.

The '1989 pattern' continued its poleward and eastward migration well after the end of 1989 when the 30-day power ended, according to Figure 9. By CR1830 (11 June 1990), the trailing end of the stream extended to about 68° latitude where the Snodgrass (1983) rotation period is 35.3 days. However, the rotation period of the mean field did not increase beyond 30 days. Thus, for latitudes above 45°, even this relatively strong field was too weak to overcome the μ^2-dependence of the mean-field integral in Eq(3), and (as we shall see in the Appendix), an extra factor of μ due to limb darkening. In the next section, we shall see that this result provides a clue for understanding some puzzling associations between the axisymmetric component of the mean field and the Sun's polar magnetic fields.

3.2.3. *Power in the Axisymmetric Component of the Sun's Mean Field*

To display the non-axisymmetric part of the mean field, B_m, we used the 27-day running mean of the standard deviation, defined by $B_m^{rms} = (< B_m^2 > - < B_m >^2)^{1/2}$, where the brackets refer to averages over a 27-day moving window. In this subsection, we are interested in $< B_m >$, the 27-day moving average of the mean field (*i.e.* the axisymmetric component that we squared and subtracted from $< B_m^2 >$ to get that non-axisymmetric component).

Another way to compare the axisymmetric and non-axisymmetric components of B_m is to express Eq(7) in terms of real variables and separate the $m = 0$ and $m \neq 0$ terms. To first order in B_0, we obtain

$$B_m \approx \left\{ \sum_{l=1}^{\infty} \rho_{l0} I_{l0} \; + \; 2 \sum_{l=1}^{\infty} \sum_{m=1}^{l} \rho_{lm} I_{lm} \cos \delta_{lm} \right\} \; + \; B_0 \left\{ \sum_{l=1}^{\infty} \rho_{l0} J_{l0} \; + \; 2 \sum_{l=1}^{\infty} \sum_{m=1}^{l} \rho_{lm} J_{lm} \cos \delta_{lm} \right\}. \tag{15}$$

Averaging over δ_{lm} (which we assume varies linearly with time, t, or more precisely with mt), we get

$$B_m^{rms} \approx \sqrt{2} \, \sqrt{\rho_{11}^2 I_{11}^2 \; + \; \rho_{22}^2 I_{22}^2 \; + \; \rho_{33}^2 I_{33}^2 \; + \rho_{31}^2 I_{31}^2} \tag{16}$$

for the root-mean-square deviation of B_m from its average value, and

$$< B_m > \; \approx \rho_{20} I_{20} \; + \; B_0 \left\{ \rho_{10} J_{10} \; + \; \rho_{30} J_{30} \right\} \tag{17}$$

for the 27-day moving average of B_m. In Eq(16), we have omitted J_{lm}-dependent terms because they occur with the second-order factor, B_0^2, and we have omitted terms with I_{21} and I_{32}, which vanish, as indicated in Table 1. Likewise, in Eq(17), we have omitted terms with I_{10}, I_{30}, and J_{20}, which also vanish as indicated in Tables 1 and 2. Thus, B_m^{rms} has non-axisymmetric ($m \neq 0$) contributions from Y_1^1, Y_2^2, Y_3^3, and Y_3^1 for which $I_{11} = +0.173$, $I_{22} = +0.103$, $I_{33} = +0.035$, and $I_{31} = -0.027$, as obtained from Table 1. In that case, we expect the non-axisymmetric component of B_m to be dominated by contributions from Y_1^1 and Y_2^2 with much smaller contributions from Y_3^3 and Y_3^1.

The axisymmetric quantity, $< B_m >$, has contributions from Y_2^0 with $I_{20} = -0.084$, plus B_0-dependent contributions from Y_1^0 and Y_3^0, with the somewhat larger values of $J_{10} = +0.244$ and $J_{30} = -0.093$. However, the factor of B_0 reduces these contributions and modulates them with a 1-year period. When B_0 has its maximum value of 7.25° (0.1265 rad), $B_0 J_{10}$ is only 0.031 (37% of I_{20}) and $B_0 J_{30}$ has the even smaller value of -0.0118 (38% of $B_0 J_{10}$). Thus, in rough terms, we can regard Y_2^0, Y_1^0, and Y_3^0 as making three monotonically decreasing contributions to the axisymmetric

part of B_m, in which each contribution is about 40% of the previous one. Now, let us see how well these terms fit the WSO mean-field measurements.

The top panel of Figure 13 contains a plot of $< B_m >$ (red) and the monthly averaged sunspot number from the Royal Observatory of Belgium (SILSO) (blue) during sunspot cycles 21 - 24. The sunspot number has been divided by

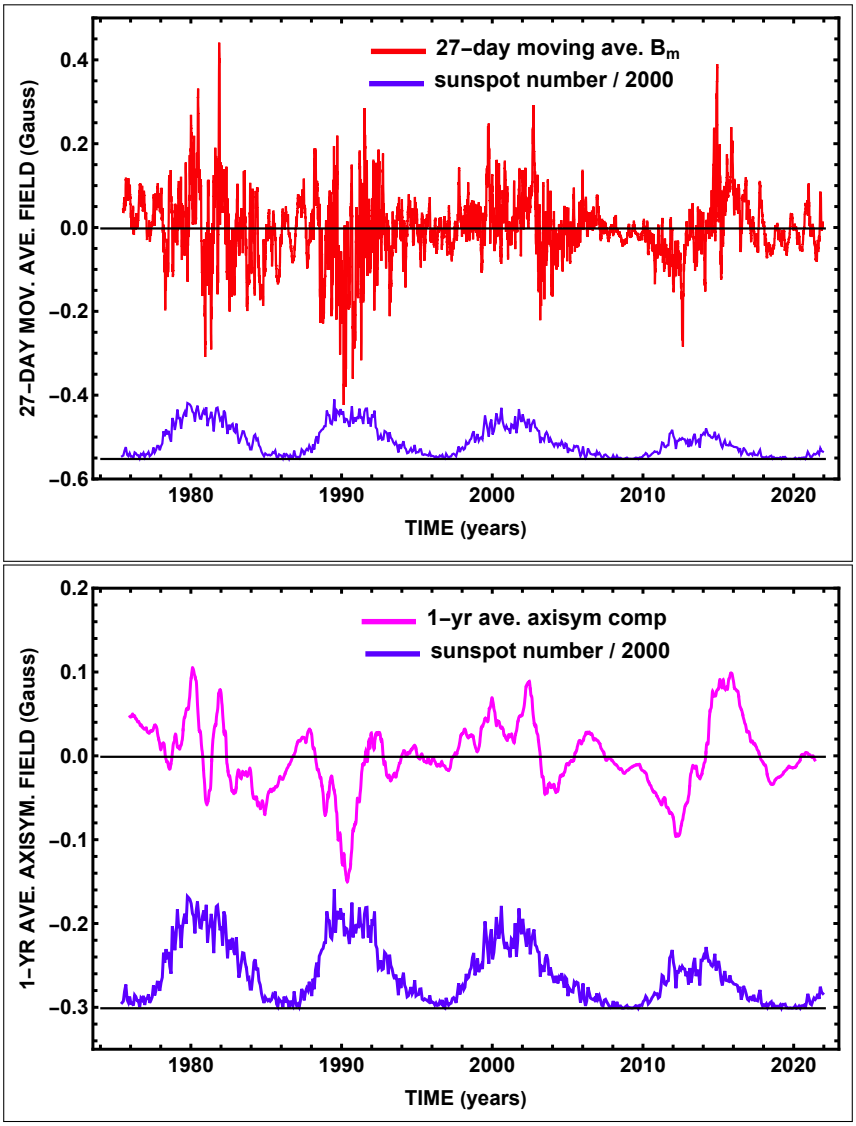

Figure 13. (top) 27-day running average of the WSO mean field (red), compared with the monthly averaged sunspot number from the Royal Observatory of Belgium (SILSO) (blue). (bottom) 365-day moving average of the red curve, showing the residual Y_2^0 component of the axisymmetric field (purple) after the annually varying Y_1^0 and Y_3^0 contributions have been removed.

2000 and shifted downward by 0.55 units on the vertical scale. At first glance, the red curve seems to be a meandering collection of relatively uninteresting noisy wiggles. However, closer inspection reveals a rough trend for the signal to be negative during the early years of sunspot maximum in sunspot cycles 22 and 24 and positive during the declining phase of those cycles. The polarities are reversed during the odd-numbered cycles 21 and 23. In addition, there are well defined annual variations during the 1976, 1986, and 2019 sunspot minima, which are presumably the most visible indications of the B_0-dependence of the axisymmetric component of the mean field as Earth orbits the Sun during the year.

These B_0-induced variations are removed in the bottom panel of Figure 13, whose purple curve is the 365-day running mean of the $< B_m >$ values associated with the red curve in the upper panel. We suppose that this purple curve

indicates the Y_2^0 contribution given by $\rho_{20} I_{20} = -0.084 \rho_{20}$ in Eq(17)[4]. Thus, the mean field reduces the contribution of the Y_2^0 component by a factor of about 12 and has a negative value corresponding to the sign of the equatorial part of a positively directed quadrupole.

The temporal profile of the purple curve in Figure 13 is similar to the profile of the Y_2^0 component calculated from spatially resolved observations at both WSO and MWO (but not shown here). The main difference occurred during 1992-1996 when the spatially resolved measurements give a much larger positive field than the mean field in Figure 13. This stronger field would have strengthened the rough, alternating-polarity rule noted from the red curve in the top panel of Figure 13.

As pointed out previously by Wang & Robbrecht (2011) and Robbrecht & Wang (2012), this polarity rule reflects the tendency of equatorial flux to originate from the leading parts of active regions together with the greater activity in the southern hemisphere than in the northern hemisphere during the declining phases of sunspot cycles 21-24. Likewise, the northern hemispheres were more active during the rising phases of those cycles. However, Wang & Robbrecht (2011) also found that this alternating-polarity rule broke down during the very high activity of sunspot cycle 19 when the northern hemisphere tended to be more active than the southern hemisphere throughout the cycle. (See also Figure 1 of White & Trotter (1977) who found no systematic variations during 1874-1971[5].)

The annually varying part of the axisymmetric field is shown by the purple curve in Figure 14. We obtained this curve

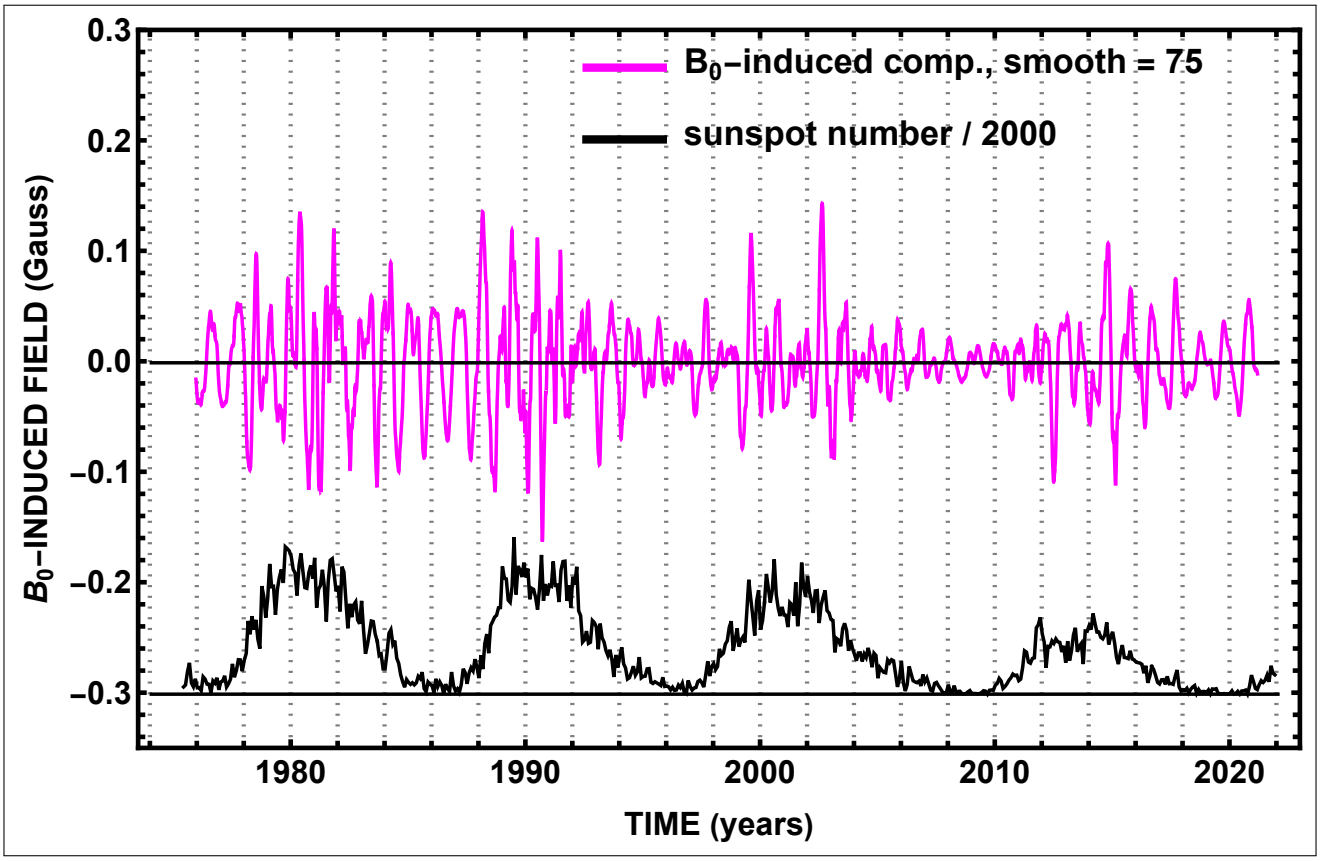

Figure 14. The axisymmetric field, $< B_m >$, with its Y_2^0 component removed and a 75-day smoothing applied to the remainder. The resulting purple curve shows annular modulation, especially during the 1976, 1986, and 2019 sunspot minima. The black curve shows the monthly averaged sunspot number from the Royal Observatory of Belgium (SILSO).

by subtracting the 1-year averaged field (purple curve in the bottom panel of Figure 13) from the total axisymmetric field (red curve in the top panel of Figure 13), and then taking a 75-day running average to remove the noise. Referring

[4] Note that Y_2^0 has the sign of its polar region, which is negative when its equatorial region is positive, according to the definition $P_2(\cos\theta) = (1/2)(3\cos^2\theta - 1)$. This accounts for the negative sign of I_{20} in Table 1.

[5] The reader may have to go to the hardcopy edition of this paper because the figure was a large foldout that was not scanned into the online edition.

to Eq(17), we expect this B_0-induced field to be $B_0(\rho_{10}J_{10} + \rho_{30}J_{30})$, where B_0 is given by

$$B_0(t) \approx 0.126 \sin\left\{2\pi\left(\frac{t-157}{365}\right)\right\} \tag{18}$$

whose amplitude vanishes on day-of-year 157 (June 6) and reaches 0.126 rad (7.25°) on day-of-year 249 (September 6), and where $J_{10} = +0.244$ and $J_{30} = -0.093$, as given in Table 2. The vertical meandering of the Y_2^0 component, that was present in the top panel of Figure 13, is clearly gone. The annual variation is strongly visible around the 1976, 1986, and 2019 sunspot minima, but only weakly visible around the 1997 and 2009 minima. Stronger non-periodic bursts occur during the intervening sunspot-maximum intervals.

Faint dotted lines have been drawn at the even-numbered years and the panels have been enlarged to help show the phase of the annual variation. For example, during 1976 and 1977, the positive peaks occurred in the fall and the negative peaks occurred in the spring, as expected for a positive axisymmetric field. In contrast, during 1985-1987, the sharp negative peaks occurred in the fall and the blunted positive peaks occurred in the spring, consistent with a negative axisymmetric field. This means that the B_0-induced axisymmetric component of the mean field changed its sign from plus to minus in going from sunspot cycle 21 to 22, in agreement with the signs of the axisymmetric dipole and the Sun's polar magnetic field. The amplitude of the B_0-induced component was much weaker during the 1997 and 2009 solar minima, but the alternation of signs was still detectable. Then in 2019, the field was strong again, and its sign was positive as expected for the continued 11-yr alternation of polarity. Thus, during the past 5 sunspot minima from 1976 to 2019, the B_0-induced component of the mean field reversed its polarity in phase with the polarity of the Sun's polar magnetic field and the Sun's axisymmetric dipole component.

Figures 15 and 16 provide more graphic displays of this phase alignment. In Figure 15, plots of the WSO polar field

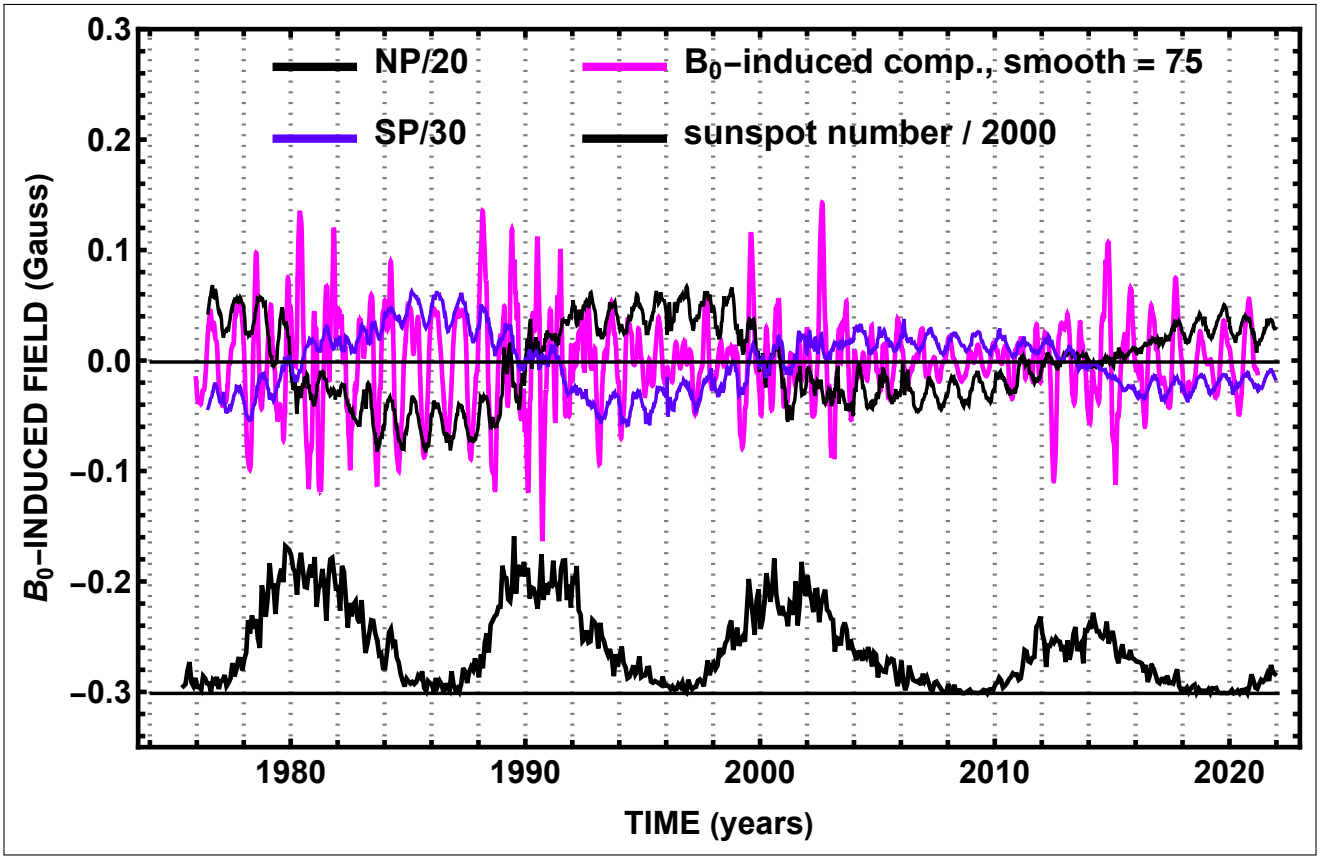

Figure 15. WSO measurements of the Sun's north (black) and south (blue) polar fields, superimposed on the smoothed plot of the B_0-induced part of the axisymmetric field (purple), and compared with the monthly-averaged sunspot number (black). Annual variations of the purple curve are in phase with the annual variations of the polar fields, but the polar fields had to be divided by separate factors of 20 and 30 to improve the agreement between the long-term envelopes of these curves.

strengths are superimposed on the B_0-induced part of the axisymmetric mean field (shown in purple again). To obtain the best overall agreement with the envelope of the mean field, I reduced the north and south polar field strengths by factors of 20 and 30, respectively, before plotting them. Now, the envelopes agree fairly well in the years around sunspot minimum, but not around sunspot maximum when the polar fields were reversing and the mean field had several large bursts. A detailed inspection of these overlapping curves shows that the annual variations of the polar fields are in sync with the annual variations of the B_0-induced field. The north polar field and its mean-field ripple reached their greatest absolute magnitudes in the fall of each year, and the south polar field and its corresponding mean-field ripple reached their greatest magnitudes in the spring.

Figure 16 provides another comparison between the B_0-induced mean field and the polar fields. In this case, the

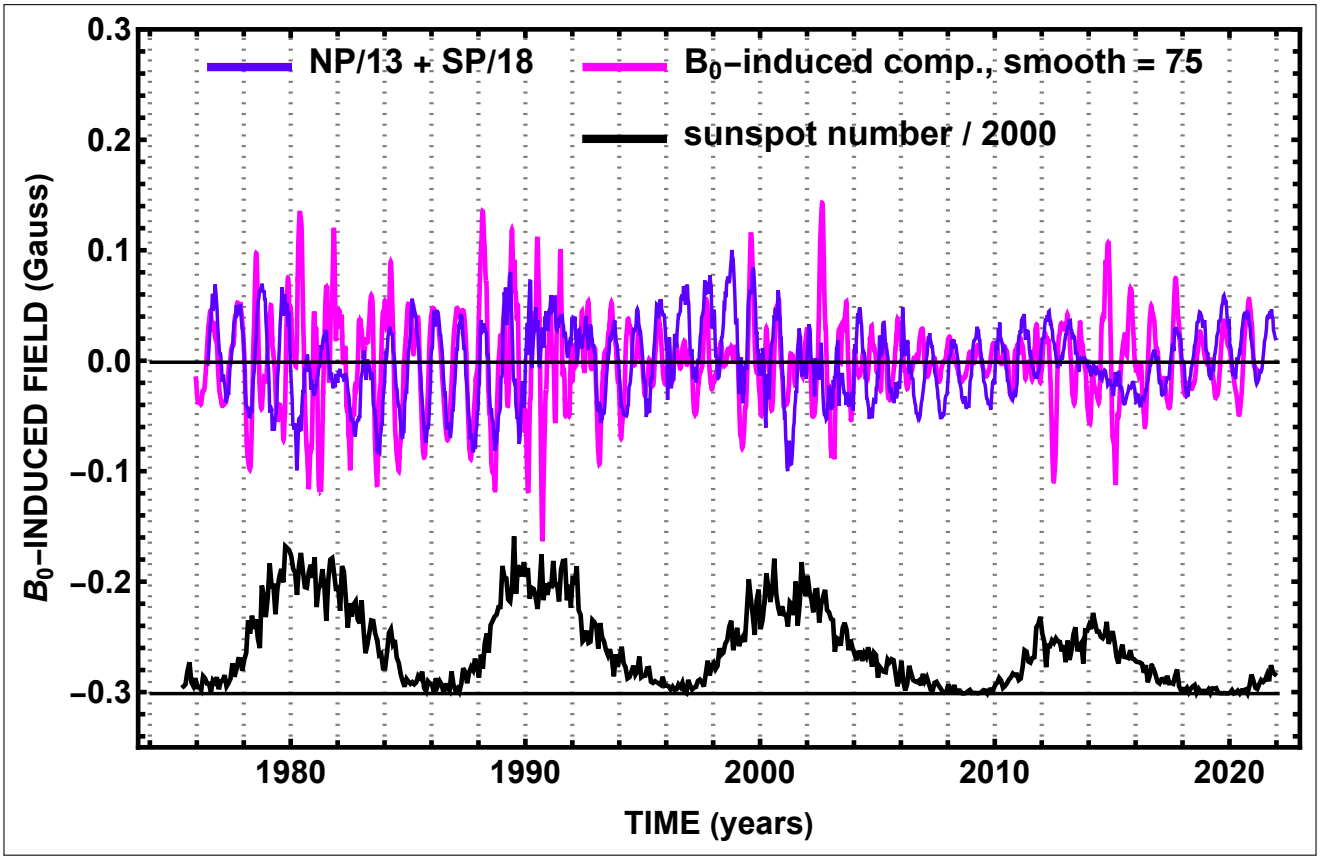

Figure 16. Weighted sum of WSO north and south polar fields (blue), superimposed on the B_0-induced part of the axisymmetric field (purple), and compared with the monthly-averaged sunspot number (black) during cycles 21 - 24. Annual variations of this sum approximately match those of the purple curve, except in the years around sunspot maximum when the polar fields reverse and the purple curve has large spikes.

weighted values of the north and south polar fields are added, to form a single oscillating blue curve similar to the overlapping purple plot of the mean field variations. Also, the weighting is changed slightly so that the contribution of the north pole is increased by a factor of $18/13 \approx 1.4$, instead of the factor of $30/20 = 1.50$ that was used in Figure 15. The overall trend is essentially the same as we found in Figure 15 with consistent agreement in phase and fair agreement in magnitude, except in the years around sunspot maximum when the polar fields changed sign and the mean field had several large purple spikes.

These graphical comparisons between the B_0-induced component of the mean field and the amplitude of the polar field clearly indicate that these two fields are in phase and that they reverse their polarities together from one sunspot cycle to the next. We might expect this phase synchronization because both of these axisymmetric fields depend strongly on Y_1^0, which reverses the polarity of its contribution from one sunspot cycle to the next.

However, the B_0-induced field and the polar field have differences that might cause their amplitudes to differ. The Y_3^0 component contributes to both fields, but with opposite signs. We have seen in Eq(17), that Y_3^0 makes a negative

contribution to the B_0-induced mean field because the coefficient, J_{30}, is negative. On the other hand, the topknot character of the polar field requires a weighted sum of the Y_1^0 and Y_3^0 contributions (and smaller contributions from Y_5^0 and Y_7^0) in order to strengthen the field at the poles and weaken the field around the equator (Svalgaard et al. 1978; DeVore et al. 1984; Sheeley et al. 1989a,b). Also, the north and south polar fields often differ in strength due to symmetry-breaking contributions from harmonic components of even l, especially the Y_2^0 component. As shown in the second column of Table 2, these even-order components do not contribute to the B_0-induced axisymmetric component of the mean field. This explains why we had to equalize the strengths of the polar fields in order to bring their plots into better agreement with the envelope of the B_0-induced axisymmetric field in Figures 15 and 16.

4. SUMMARY AND DISCUSSION

In this paper, I have regarded the Sun as an unresolved source of light like that from a distant star, and calculated the transmission that this 'mean-field filter' would have for the spherical harmonic components, Y_l^m, of the field. This transmission depends on the mode numbers, l and m, and B_0, the observer's latitude in the star's polar coordinate system. The transmissions fell into three separate classes, proportional to $\cos^2 B_0$, $(\sin 2B_0)/2$, and $\sin^2 B_0$, as given in Tables 1-3, respectively, and described in Eqs(5) and (7). For the Sun, B_0 varies between $-7.^\circ25$ and $+7.^\circ25$ during the year, so that $\sin^2 B_0$ is small and Table 3 can be neglected. In that case, we expect the axisymmetric part of the mean field to originate from the Y_2^0 component and the first few harmonic components of odd l (mainly Y_1^0 and Y_3^0), which are related to the polar fields and are coupled to the mean field *via* B_0. On the other hand, we expect the non-axisymmetric part of the mean field to originate from the Y_1^1 and Y_2^2 components with occasional small contributions from the Y_3^3 and Y_3^1 components.

For our observations of the Sun, B_0 is small and the contribution of the Y_2^0 component comes from its equatorial band, which is negative for a positively defined Y_2^0 component. This is why the sign of I_{20} is negative in Table 1. On the other hand, for a distant star observed nearly head-on, B_0 would be $\sim 90^\circ$, and the Y_2^0 contribution would come from one of its two polar regions of positive polarity. This is why the sign of K_{20} is positive in Table 3.

I applied these ideas to the 46-year series of WSO daily measurements of the Sun's line-of-sight mean field, first plotting the 27-day running average of the rms deviation of the mean field from its average value. This rms variation provided a measure of the power in the non-axisymmetric components of the field, and showed peaks already familiar to us from plots of the occurrence of coronal inflows, of the Sun's open flux and interplanetary magnetic field, of the Sun's equatorial dipole and quadrupole field, of the non-axisymmetric component of the Sun's source-surface magnetic field, and of the mean field represented by a running 27-day average of its maximum-minus-minimum values (Sheeley & Wang 2014, 2015). In retrospect, this similarity of plots should be no surprise because they all show peaks corresponding to the envelope of the non-axisymmetric component of the Sun's large-scale field as it is modulated by solar rotation, analogous to the audio component of a high-frequency radio wave.

The second step was to take the Fourier transform of the mean-field measurements and display power as a function of frequency. The result was a series of peaks at frequencies corresponding to the 27-day synodic solar rotation period and its first two harmonics. In addition, each peak showed fine structure at slightly longer periods, corresponding to the Sun's rotation at higher latitudes. By inverting this Fourier transform using broad windows around these three peaks, I obtained a relatively noise-free version of the non-axisymmetric mean field. In addition, temporal plots of the $m = 1$, $m = 2$, and $m = 3$ components of the non-axisymmetric field were obtained by selecting each of the three windows separately. By comparing these plots with the temporal plot of their sum, we learned that nearly all of the large peaks were provided by the combination of $m = 1$ and $m = 2$ plus a few residual contributions of $m = 3$. In other words, the mean field is dominated by the Y_1^1 and Y_2^2 components of the field, consistent with our analysis of Eq(16).

The third step was to find the source of the fine structure in the power spectrum, and in particular of the peak whose frequency corresponded to a period of ~30 days. This narrow peak was particularly interesting because it had no counterpart in the interplanetary sector structure inferred from Earth-based magnetometer measurements. Those in-ecliptic measurements often show 28.5-day recurrence patterns, but never 30-day patterns.

By inverting the Fourier transform of the mean field through a narrow window around the 30-day peak, I found that most of the power originated in 1989-1990 when photospheric magnetograms showed elongated patterns of magnetic fields migrating to high latitudes in the northern hemisphere. This reminds us that the mean-field is sampling large-scale magnetic patterns, which gradually rotate rigidly as supergranular diffusion and meridional flow carry their flux across latitudes (Sheeley et al. 1987; DeVore 1987; Wang 1998). Thus, mean-field measurements give the pattern rate,

which depends on the meridional transport parameters as well as the rate of differential rotation, and not just the rotation rate itself. We are still left with the interesting quantitative question of why the 1989-1990 fields gave a rotation period of ∼30 days, rather than a longer period associated with the high-latitude tail of the migrating stream or the shorter, ∼28.5-day period found for so many other migrating streams.

If the answer lies in the strength of the active region that emerged at 35°N latitude in 1989, then we might ask if similar (or even stronger) active regions may have emerged at high latitudes in previous sunspot cycles, like cycles 18 and 19, that were more active than cycles 21 - 24. A large northern-hemisphere pattern was visible in Ca II K-line maps and Fe I 5250 Å magnetograms obtained at the Mount Wilson Observatory during Carrington rotations 1417 (8 August - 4 September, 1959) and 1419 (2-29 October 1959) (Sheeley et al. 2011). Another occurred in the southern hemisphere during rotations 1259 (21 October - 17 November 1947) and 1261 (14 December 1947 - 11 January 1948). Perhaps those migrating fields would have produced $m = 1$ sidebands with rotation periods of at least 30 days in the power spectrum of the mean field.

The fourth step was to look at the axisymmetric component of the mean field. This component consisted of the Y_2^0 component plus the strongest B_0-induced components of odd l, mainly Y_1^0 and Y_3^0. Because B_0 varies annually due to Earth's orbital motion around the Sun, it was possible to remove the B_0-induced term, and display the annually averaged Y_2^0 component separately. Although not shown here, its temporal profile was similar to those obtained from spatially resolved observations at both WSO and MWO, except for the interval 1992-1996 when the spatially resolved measurements gave a much larger positive field. Resolving this discrepancy will be a challenge for the future.

Once the Y_2^0 component was found, it was then possible to extract the B_0-induced part of the axisymmetric field. Its annual variation was in phase with the annual variation of the polar magnetic fields. This means that the B_0-induced field was oriented in the same direction as the polar field, reversing its direction from one sunspot cycle to the next. A remaining puzzle is why the annual variations were strong around the 2019 sunspot minimum when the polar fields were weak, and why the annual variations were weak around the 1997 minimum when the polar fields were stronger.

Finally, we note that this approach can be used to find spherical harmonic components of the fields in other stars. For example, the B_0-dependence of the strengths of these harmonic components may complement asteroseismology determinations of the orientations of the rotational axes of these stars (Gizon & Solanki 2003). Also, the appearance of low-frequency sidebands in the WSO spectra suggests that similar sidebands may occur in observations of other stars, providing information about differential rotation and meridional flow in those stars. This information may help to remove ambiguities in the inferences of large scale convection and magnetic cycles in asteroseismology studies of Sun-like stars.

ACKNOWLEDGMENTS

I am grateful to Phil Scherrer (WSO/Stanford) and Todd Hoeksema (WSO/Stanford) for helpful comments about the WSO telescope and its data, and Yi-Ming Wang (NRL) for numerous discussions of the Sun's large-scale magnetic field. I am grateful to Jack Harvey (NSO/LPL/UA) for helping me find archived Carrington maps of observations obtained with the Kitt Peak Vacuum Telescope. This work evolved from a talk that I gave at an LPL/UA Heliophysics Group Zoom session where Joe Giacalone, Jack Harvey, and John Leibacher provided useful comments and ideas. Wilcox Solar Observatory data used in this study were obtained *via* the web site http://wso.stanford.edu courtesy of J.T. Hoeksema. NSO data were acquired by SOLIS instruments operated by NISP/NSO/AURA/NSF. Sunspot numbers were obtained from WDC-SILSO, Royal Observatory of Belgium, Brussels. I am grateful to the referee for several helpful comments, including one about limb darkening which motivated the calculations in the Appendix.

APPENDIX

A. LIMB DARKENING

In Section 2, we converted the integral of the line-of-sight field over the (flat) solar disk to a surface integral of the radial field over the visible hemisphere. As shown in Eq(3), this conversion introduced two factors of μ into the integrand, causing the surface integral of B_r to be weighted toward the disk center by a factor of μ^2. However, we did not include the natural weighting that is produced by the limb darkening of the Sun and stars in the visual region

of the spectrum. This limb darkening occurs because light from disk center originates in deeper, hotter, and brighter layers than light from positions toward the limb. As described by Scherrer et al. (1977a), the central weighting of the WSO measurements is mainly due to this natural limb darkening plus a contribution of diffraction from the entrance slit of the spectrograph.

It is relatively easy to include limb darkening in our equations for the mean line-of-sight magnetic field. We simply insert the limb darkening intensity profile, $I(\mu)/I(0)$, next to the μ^2 in the integrand of Eq (3). With the definition $F(\mu) = I(\mu)/I(0)$, Eq(3) becomes

$$B_m \;=\; \int B_r \mu^2 F(\mu) dA_{surf}/\pi R^2. \tag{A1}$$

Then, we replace μ by $\sin\theta\cos\phi\cos B_0 + \cos\theta\sin B_0$, and perform the integration over the variables θ and ϕ as indicated in Eqs(4) and (5). If $F(\mu)$ is a simple first- or second-order polynomial in μ, one can do the integration analytically, but if the profile is more complicated, then it might be more convenient to integrate numerically.

Let's begin by considering some of the limb darkening relations that are used to describe the Sun and stars. Classically, the natural limb darkening has been described by a linear function of μ of the form

$$\frac{I(\mu)}{I(0)} \;=\; 1 - \gamma(1-\mu) = (1-\gamma) + \gamma\mu. \tag{A2}$$

Here, γ is a wavelength-dependent limb-darkening coefficient that indicates how dark the limb is relative to the disk center at that wavelength. For the so-called gray atmosphere in the Eddington approximation (Foukal 1990; Schwarzschild 1906), $\gamma = 0.6$ and $I(\mu)/I(0) = 0.4 + 0.6\mu$. According to Maxted (2018), Kopal's (1950) quadratic limb darkening relation of the form

$$\frac{I(\mu)}{I(0)} \;=\; 1 - c_1(1-\mu) - c_2(1-\mu)^2 \tag{A3}$$

is the most commonly used profile in modern exoplanet studies. Stellar limb darkening is important in these studies because it affects the light curve produced by the transiting exoplanet and therefore the accuracy with which the exoplanetary radius can be determined. Consequently, other profiles are sometimes used to match the high-precision light curves of transiting exoplanet systems (Knutson et al. 2007; Espinoza & Jordán 2015). In particular, Maxted (2018) considered another two-parameter limb-darkening relation of the form

$$\frac{I(\mu)}{I(0)} \;=\; 1 - c(1-\mu^\alpha). \tag{A4}$$

Although any of these limb darkening relations can be substituted into Eq(A1) above, I will illustrate the procedure using the linear relation given by Eq(A2). In this case, B_m can be obtained from proportionate parts of Eq(4) and of the modified version of Eq(4) when an extra factor of μ is included in its integrand. This latter quantity, which I call B_μ to distinguish it from B_m, is given by

$$B_\mu \;=\; (1/\pi)\int_{-\pi/2}^{\pi/2}\int_0^{\pi} B_r(\sin\theta\cos\phi\cos B_0 + \cos\theta\sin B_0)^3 \sin\theta d\theta d\phi. \tag{A5}$$

The third-power expansion of this binomial expression for μ gives four terms with factors of $\cos^3 B_0$, $3\cos^2 B_0 \sin B_0$, $3\cos B_0 \sin^2 B_0$, and $\sin^3 B_0$, respectively, instead of the three terms that we obtained from the second-power expansion of that binomial in Eq(4).

It would be easy to evaluate all four integrals and put the results in tables as we did in the main text. However, to estimate the effect of limb darkening on the mean field of the Sun, it is sufficient to expand the B_0-dependent factors in powers of B_0 and retain only the zeroth-order and first-order terms. This means that we need to keep only the $\cos^3 B_0$ and $3\cos^2 B_0 \sin B_0$ factors, which reduce to 1 and $3B_0$, respectively. Then, the limb darkened mean field becomes

$$B_m \;=\; (1-\gamma)(I_{lm} + B_0 J_{lm}) \;+\; \gamma(I^\mu_{lm} + B_0 J^\mu_{lm}), \tag{A6}$$

where the terms that originate from Eq(A5) are given by

$$I^\mu_{lm} \;=\; \frac{N_{lm}}{\pi}\int_{-1}^{1} P_l^m(x)(1-x^2)^{3/2} dx \left[\frac{12\cos(m\pi/2)}{(m+1)(m-1)(m+3)(m-3)}\right], \tag{A7a}$$

$$J^\mu_{lm} \;=\; 3\frac{N_{lm}}{\pi}\int_{-1}^{1} P_l^m(x)(1-x^2) x dx \left[\frac{-4\sin(m\pi/2)}{m(m+2)(m-2)}\right]. \tag{A7b}$$

Next, we rearrange Eq(A6) as a power series in B_0 to obtain

$$B_m \;=\; \{(1-\gamma)I_{lm} + \gamma I^{\mu}_{lm}\} \;+\; B_0\{(1-\gamma)J_{lm} + \gamma J^{\mu}_{lm}\}. \tag{A8}$$

I used the conventional Mathematica software to evaluate I^{μ}_{lm} and J^{μ}_{lm} for l and m in the range $0-7$, again reversing the signs of the odd-m entries to be consistent with the Jahnke & Emde (1945)-convention. Then I set $\gamma = 0.6$, and combined these results with the values of I_{lm} and J_{lm} given in Tables 1 and 2 to obtain the limb darkened intensities for the gray atmosphere in the Eddington approximation. The results are given in Tables 4 and 5.

Table 4. Limb-Darkened Elements of B_{lm} {zeroth-order in B_0}

l/m	0	1	2	3	4	5	6	7
0	+0.160							
1	0	+0.152						
2	-0.081	0	+0.099					
3	0	-0.033	0	+0.043				
4	+0.006	0	-0.006	0	+0.008			
5	0	-0.001	0	+0.002	0	-0.002		
6	+0.001	0	-0.001	0	+0.001	0	-0.001	
7	0	-0.000	0	+0.000	0	-0.000	0	+0.001

Table 5. Limb-Darkened Elements of B_{lm} {first-order in B_0}

l/m	0	1	2	3	4	5	6	7
0	0							
1	+0.215	0						
2	0	+0.198	0					
3	-0.114	0	+0.104	0				
4	0	-0.026	0	+0.023	0			
5	-0.007	0	+0.007	0	-0.006	0		
6	0	-0.004	0	+0.004	0	-0.003	0	
7	-0.003	0	+0.003	0	-0.003	0	+0.002	0

Comparing Table 1 and Table 4, we see that the elements have the same sign and nearly the same magnitude for $l < 4$. For larger values of l, there are some sign differences, especially for $l = 4$ and $l = 6$, but the magnitudes of these higher-order harmonic components are less than 0.01 and can be neglected. A comparison between Tables 2 and 5 gives a similar result. This means that the same harmonic components contribute to the mean field with or without limb darkening, but that the strengths of these contributions differ slightly, depending on the values of γ and l (as we shall see next).

We can gain further insight by computing the relative differences between these limb-darkened and non-limb-darkened intensities. Doing this separately for the terms that are zero-order and first-order in B_0, we obtain

$$(\frac{\Delta B}{B})_0 = \frac{\{(1-\gamma)I_{lm} + \gamma I^{\mu}_{lm}\} - I_{lm}}{I_{lm}} = -\gamma(1 - \frac{I^{\mu}_{lm}}{I_{lm}}) \quad \text{(A9)}$$

and

$$(\frac{\Delta B}{B})_1 = \frac{\{(1-\gamma)J_{lm} + \gamma J^{\mu}_{lm}\} - J_{lm}}{J_{lm}} = -\gamma(1 - \frac{J^{\mu}_{lm}}{J_{lm}}). \quad \text{(A10)}$$

Thus, the zeroth-order change, $(\Delta B/B)_0$, depends on the ratio I^{μ}_{lm}/I_{lm}, and the first-order change, $(\Delta B/B)_1$, depends on the ratio J^{μ}_{lm}/J_{lm}. And both changes are proportional to the limb darkening coefficient, γ. Moreover, if we use Eqs(A7ab) and Eqs(11ab) to evaluate the ratios, I^{μ}_{lm}/I_{lm} and J^{μ}_{lm}/J_{lm}, we obtain the remarkable result that the values of these ratios are the rational numbers 4/5, 15/16, and 48/35, for $l = 1$, 2, and 3, respectively, independent of the values of m. (Of course, this applies only for the non-zero values of I_{lm} and J_{lm} in Tables 1 and 2, respectively.)

In other words, for the Y^0_1 and Y^1_1 harmonics, the ratios, J^{μ}_{10}/J_{10} and I^{μ}_{11}/I_{11}, are both equal to 4/5. Likewise, for the Y^0_2, Y^1_2, and Y^2_2 harmonics, the ratios are all equal to 15/16. And for the four harmonics with $l = 3$, the ratios are 48/35. Subtracting these ratios from 1, we obtain 1/5, 1/16, and -13/35, as the fractional differences in Eqs(A9) and (A10) for $l = 1$, 2, and 3, respectively, before the limb darkening factor, γ, is applied.

If we let $\gamma = 0.6$, we obtain changes of -12%, -3.75%, and +22.2%, for $l = 1$, 2, and 3, respectively, independent of the value of m. Thus, for an ideal gray atmosphere in the Eddington approximation, the amplitudes of the Y^0_1 and Y^1_1 components decrease by 12%. The three components with $l = 2$ decrease by only 3.75% and the four relatively weak components with $l = 3$ go in the opposite direction, increasing by 22.2%.

The nice aspect of Eqs(A9) and (A10) is that we can increase γ to obtain the fractional changes for a greater amount of limb darkening in the violet part of the spectrum, or decrease γ to obtain the smaller changes expected in the infrared. We simply return to the fractions 1/5, 1/16, and -13/35 and multiply them by $-\gamma$.

I did this calculation to learn how solar limb darkening in the simple Eddington approximation might affect the harmonic components of the mean field. However, for more complex limb darkening profiles and the more inclined rotational axes, that might occur in exoplanet or asteroseismic studies, one could relax the small-B_0 approximation used for the Sun, and do the integration numerically for specific values of B_0. We might expect limb darkening to have a more complicated effect for a star whose rotational axis makes an oblique angle to the line of sight.

REFERENCES

Boteler, D. H. 2019, Space Weather, 17, 1427, doi: 10.1029/2019SW002278

DeVore, C. R. 1987, SoPh, 112, 17, doi: 10.1007/BF00148484

DeVore, C. R., Boris, J. P., & Sheeley, N. R., J. 1984, SoPh, 92, 1, doi: 10.1007/BF00157230

Espinoza, N., & Jordán, A. 2015, MNRAS, 450, 1879, doi: 10.1093/mnras/stv744

Foukal, P. 1990, Solar astrophysics

Gizon, L., & Solanki, S. K. 2003, ApJ, 589, 1009, doi: 10.1086/374715

Hoeksema, J. T. 1984, PhD thesis, Stanford Univ., CA.

Jahnke, E., & Emde, F. 1945, Tables of Functions with Formulae and Curves (4th Edition) (New York: Dover Publications)

Jones, D. E. 1972, The Interplanetary and Solar Magnetic Field Sector Structures, 1962-1968, ed. C. P. Sonett, P. J. Coleman, & J. M. Wilcox, Vol. 308, 122

Knutson, H. A., Charbonneau, D., Noyes, R. W., Brown, T. M., & Gilliland, R. L. 2007, ApJ, 655, 564, doi: 10.1086/510111

Kopal, Z. 1950, Harvard College Observatory Circular, 454, 1

Kotov, V. A. 2019, Ap&SS, 364, 45, doi: 10.1007/s10509-019-3534-z

Maxted, P. F. L. 2018, A&A, 616, A39, doi: 10.1051/0004-6361/201832944

Ness, N. F., & Wilcox, J. M. 1965, Science, 148, 1592, doi: 10.1126/science.148.3677.1592

Robbrecht, E., & Wang, Y. M. 2012, ApJ, 755, 135, doi: 10.1088/0004-637X/755/2/135

Sanchez-Diaz, E., Rouillard, A. P., Davies, J. A., et al. 2017, ApJL, 835, L7, doi: 10.3847/2041-8213/835/1/L7

Scherrer, P. H., Duvall, T. L., J., Dittmer, P. H., Gustafson, E. K., & Wilcox, J. M. 1976, in Bulletin of the American Astronomical Society, Vol. 8, 370

Scherrer, P. H., Wilcox, J. M., Kotov, V., Severny, A. B., & Howard, R. 1977a, SoPh, 52, vi, doi: 10.1007/BF00935783
Scherrer, P. H., Wilcox, J. M., Svalgaard, L., et al. 1977b, SoPh, 54, 353, doi: 10.1007/BF00159925
Schwarzschild, K. 1906, Nachrichten von der Königlichen Gesellschaft der Wissenschaften zu Göttingen. Math.-phys. Klasse, 195, 41
Sheeley, N. R., J., Cooper, T. J., & Anderson, J. R. L. 2011, ApJ, 730, 51, doi: 10.1088/0004-637X/730/1/51
Sheeley, N. R., J., & DeVore, C. R. 1986a, SoPh, 103, 203, doi: 10.1007/BF00147824
—. 1986b, SoPh, 104, 425, doi: 10.1007/BF00159092
Sheeley, N. R., J., DeVore, C. R., & Boris, J. P. 1985, SoPh, 98, 219, doi: 10.1007/BF00152457
Sheeley, N. R., J., Harvey, J. W., & Feldman, W. C. 1976, SoPh, 49, 271, doi: 10.1007/BF00162451
Sheeley, N. R., J., Nash, A. G., & Wang, Y. M. 1987, ApJ, 319, 481, doi: 10.1086/165472
Sheeley, N. R., J., & Rouillard, A. P. 2010, ApJ, 715, 300, doi: 10.1088/0004-637X/715/1/300
Sheeley, N. R., J., & Wang, Y. M. 2014, ApJ, 797, 10, doi: 10.1088/0004-637X/797/1/10
—. 2015, ApJ, 809, 113, doi: 10.1088/0004-637X/809/2/113
Sheeley, N. R., J., Wang, Y. M., & DeVore, C. R. 1989a, SoPh, 124, 1, doi: 10.1007/BF00146515
Sheeley, N. R., J., Herbst, A. D., Palatchi, C. A., et al. 2008a, ApJL, 674, L109, doi: 10.1086/529020
—. 2008b, ApJ, 675, 853, doi: 10.1086/526422
Sheeley, N. R., Wang, Y. M., & Harvey, J. W. 1989b, SoPh, 119, 323, doi: 10.1007/BF00146182
Snodgrass, H. B. 1983, ApJ, 270, 288, doi: 10.1086/161121
Svalgaard, L., Duvall, T. L., J., & Scherrer, P. H. 1978, SoPh, 58, 225, doi: 10.1007/BF00157268
Svalgaard, L., & Wilcox, J. M. 1975, SoPh, 41, 461, doi: 10.1007/BF00154083
Wang, Y. M. 1998, in Astronomical Society of the Pacific Conference Series, Vol. 154, Cool Stars, Stellar Systems, and the Sun, ed. R. A. Donahue & J. A. Bookbinder, 131
Wang, Y. M., & Hess, P. 2018, ApJ, 859, 135, doi: 10.3847/1538-4357/aabfd5
Wang, Y. M., & Robbrecht, E. 2011, ApJ, 736, 136, doi: 10.1088/0004-637X/736/2/136
Wang, Y. M., & Sheeley, N. R., J. 1994a, ApJ, 430, 399, doi: 10.1086/174415
—. 1994b, J. Geophys. Res., 99, 6597, doi: 10.1029/93JA02105
White, O. R., & Trotter, D. E. 1977, ApJS, 33, 391, doi: 10.1086/190432
Wilcox, J. M., & Howard, R. 1968, SoPh, 5, 564, doi: 10.1007/BF00147021
Wilcox, J. M., & Ness, N. F. 1965a, in International Cosmic Ray Conference, Vol. 1, International Cosmic Ray Conference, 302
Wilcox, J. M., & Ness, N. F. 1965b, J. Geophys. Res., 70, 5793, doi: 10.1029/JZ070i023p05793
Wolfram, S. 1999, The Mathematica Book (4th Edition) (USA: Cambridge University Press)